Applied Catalysis B: Environment and Energy 374 (2025) 125394

Contents lists available at ScienceDirect

Applied Catalysis B: Environment and Energy

journal homepage: www.elsevier.com/locate/apcatb

Epitaxial $Bi_4O_5Br_2$ nanosheets on hollow carbon spheres for confined electron pump reactor and enhanced photocatalytic CO_2 hydrogenation reduction

Bin Wang [a,b,c], Hailong Chen [d], Fangcheng Huang [f], Jinyuan Liu [a,b], Gaopeng Liu [a], Yu-Xiang Weng [d], Yuanbin She [e], Xingwang Zhu [c,*], Huaming Li [a], Jiexiang Xia [a,*], Paul K. Chu [b,*]

[a] School of Chemistry and Chemical Engineering, Institute for Energy Research, Jiangsu University, 301 Xuefu Road, Zhenjiang 212013, PR China
[b] Department of Physics, Department of Materials Science and Engineering, and Department of Biomedical Engineering, City University of Hong Kong, Kowloon 999077, Hong Kong
[c] Institute of Technology for Carbon Neutralization, College of Environmental Science and Engineering, Yangzhou University, Yangzhou 225009, PR China
[d] Beijing National Laboratory for Condensed Matter Physics, CAS Key Laboratory of Soft Matter Physics, Institute of Physics, Chinese Academy of Sciences, Beijing 100190, PR China
[e] College of Chemical Engineering, Zhejiang University of Technology, Hangzhou, Zhejiang 310014, PR China
[f] Department of Information Engineering, Electronics, and Telecommunications, Sapienza University of Rome, Piazzale Aldo Moro 5, Roma 00185, Italy

ARTICLE INFO

Keywords:
$Bi_4O_5Br_2$
Hollow carbon spheres
Photocatalysis
CO_2 reduction
Electron pump reactor

ABSTRACT

In order to enhance the efficiency of artificial photosynthesis, it is imperative to improve the hysteretic migration and separation efficiency of photogenerated charge carriers. Herein, ultrathin $Bi_4O_5Br_2$ (BOB) nanosheets are prepared vertically and uniformly on the surface of hollow N-doped carbon spheres (NC) to produce a hollow confined nanoreactor (BOB@NC). The graphite layer and N in NC act as a tandem electron pump for the rapid transfer of photogenerated electrons from BOB to the NC surface *via* the Bi-C bridging bond between BOB and NC, and the electrons on the NC surface continue to move to the N-induced defect energy levels. This NC electron pump facilitates the transfer of the photogenerated electrons in a directional, rapid, and efficient manner. Meanwhile, the adsorption of CO_2 molecules and hydrogenation of *CO to *CHO at the N site on NC are kinetically spontaneous, thereby significantly reducing the CO_2 reduction reaction energy barrier of BOB. As a result, the efficiency of CO_2 hydrogenation reduction to CO and CH_4 by BOB@NC is 3.31 and 11.15 times higher than that by the BOB monomer, respectively. The hollow confined electron pump reactor reveals a novel strategy for the design and fabrication of catalysts for high-performance artificial photosynthesis.

1. Introduction

Simulating plant photosynthesis and converting greenhouse gas CO_2 into carbon-based fuels using clean solar energy is a cutting-edge approach to mitigating fossil fuel consumption and environmental pollution [1,2]. Since CO_2 is a stable molecule with a C═O bond energy of 750 kJ mol^{-1} [3], traditional CO_2 reduction is plagued by the low photogenerated carrier separation efficiency and low-efficiency CO_2 adsorption-activation-hydrogenation sites on photocatalysts [4,5]. Therefore, a photocatalyst that combines effective directional separation of photogenerated carriers, efficient CO_2 activation, and abundant reduction sites is crucial to the development of artificial photosynthesis.

Traditional modification strategies such as morphological control, defect engineering, and heterostructure construction can improve the photocatalytic CO_2 reduction performance to a certain extent [6–9]. Morphological control and defect engineering are structural. Although surface modification of monomer materials can increase the number of active sites, photogenerated carriers can recombine easily in the bulk and on the surface [10,11]. Heterostructure construction can build paths for photogenerated electron migration, but it is necessary to avoid the heterojunction becoming a recombination center for photogenerated carriers and the migration direction of photogenerated electrons being

* Corresponding authors.
E-mail addresses: zxw@yzu.edu.cn (X. Zhu), xjx@ujs.edu.cn (J. Xia), paul.chu@cityu.edu.hk (P.K. Chu).

https://doi.org/10.1016/j.apcatb.2025.125394
Received 26 December 2024; Received in revised form 10 April 2025; Accepted 19 April 2025
Available online 21 April 2025

opposite to the active sites [12,13]. Therefore, by combining the morphological and structural characteristics (e.g., band structure, defect structure) of nanomaterials with different dimensions, a composite photocatalyst can be designed that aligns the directional migration-enrichment of photogenerated electrons with CO_2 adsorption-activation sites. This approach is expected to maximize the utilization of photogenerated electrons and enhance CO_2 conversion efficiency.

Hollow nanostructures have received much attention in photocatalysis because the large specific surface area promotes the adsorption and activation of CO_2, and a local high-concentration CO_2 region can be formed inside the cavity [14,15]. The surface CO_2-philic functional groups (amino, hydroxyl, etc.) or heteroatoms (N, S, O, etc.) can greatly improve the enrichment efficiency of reactants [16,17]. Meanwhile, the hollow structure can reflect and scatter incident light multiple times through the internal cavity, extend the light propagation path, and significantly improve the light absorption efficiency [18]. Among the various types of hollow nanomaterials, hollow carbon spheres have advantages such as their open structure, high conductivity, good chemical stability, and tunable surface properties [19]. Since carbonaceous materials can have metallic properties, the lifetime of photogenerated hot electrons is short. On the other hand, they have high electrical conductivity and unique electron pumping properties, thus facilitating the separation of photogenerated electrons [20,21]. For instance, semiconducting materials with suitable band structures have been prepared on the outer wall of hollow carbon spheres to form confined electron pump reactors [22], in which photogenerated electrons from the semiconductor migrate directionally to hollow carbon spheres to capture CO_2 molecules and improve the CO_2 reduction efficiency. Bai et al. have deposited CdS nanoparticles on hollow carbon spheres and coated them with $ZnIn_2S_4$ layers to generate a three-component structure C/CdS@$ZnIn_2S_4$ photocatalyst with improved catalytic activity, selectivity, and stability in photocatalytic CO_2 reduction to CO [20]. Yu et al. Have constructed TiO_2/N-doped graphene (NG) hollow sphere photocatalysts by chemical vapor deposition. The close interfacial contact between TiO_2 and NG and abundant pyridinic N sites on the surface of NG promote the separation and transport of photogenerated carriers to enhance photocatalytic CO_2 reduction [23]. The synergistic functions of hollow carbon sphere materials and semiconductors provide a new pathway for efficient light absorption and CO_2 adsorption-activation-conversion for photocatalytic CO_2 reduction.

$Bi_4O_5Br_2$ (BOB) is a semiconductor with a unique V-VI-VII layered crystal structure and optical properties [24,25]. It can be excited by visible light to generate photogenerated carriers. The separation of photogenerated electrons and holes can be improved under the action of the electrostatic field generated vertically inside the crystal [26,27]. However, in monomer materials, the separation efficiency of photogenerated electrons/holes is low, and a large number of photogenerated carriers recombine both on the surface and in the bulk [24,28]. In order to optimize the directional migration and separation efficiency of photogenerated carriers of BOB and improve the photocatalytic characteristics, modification strategies such as S/Z-scheme heterojunction [29,30], defect engineering [26,31], and metal/non-metal doping [32,33], lattice distortion [34] have been proposed. By combining the unique structure and photoelectrochemical properties of hollow carbon spheres, BOB nanosheets can be prepared on the outer wall of hollow carbon spheres. The photogenerated electrons on the BOB nanosheets migrate to the surface of the carbon spheres with unique electronic pumping properties to improve the photogenerated carrier separation efficiency. Nonetheless, the success of this strategy has not been reported, and an in-depth understanding of the pertinent mechanism is still lacking from the perspective of artificial photosynthesis.

Herein, epitaxial BOB nanosheets on hollow nitrogen-doped carbon spheres (BOB@NC) are prepared controllably to form a confined electron pump nanoreactor. The ultrathin BOB nanosheets are loaded and upright uniformly on the outer surface of NC. By conducting systematic theoretical calculation of the band structure and electron distribution, excited state simulation, ultrafast femtosecond laser analysis, and optoelectronic characterization, the photo-generated electrons from BOB nanosheets are found to converge from the surface to the edge upon light excitation, and the edge electrons migrate to the NC electron pump surface *via* the Bi-C bridge bonds. The photogenerated electrons on NC rapidly undergo e-h exciton state generation and transfer to N-induced defect states, consequently separating the photogenerated electrons from BOB. In this case, NC acts as the photogenerated electron enrichment center and also traps CO_2 molecules in the cavity. Meanwhile, the N atoms in NC serve as the main active sites for spontaneous adsorption-activation of CO_2, leading to the effective reduction of the energy barrier for the generation of the key intermediate product of *COOH. Contrary to the BOB monomer, the intermediate product *CO desorbs to generate CO gas from the N site on BOB@NC *via* an endothermic reaction, while the hydrogenation of *CO to *CHO is a spontaneous exothermic reaction, which significantly increases the probability of BOB@NC reduction CO_2 and generation of CH_4 products. As a result, the efficiency of BOB@NC in reducing CO_2 to CO and CH_4 is 3.31 and 11.15 times that of BOB, respectively.

2. Experimental section

2.1. Materials and chemicals

Tetraethyl orthosilicate (TEOS), ethanol, aqueous ammonia (28 wt %), ammonium hydrogen fluoride (NH_4HF_2), bismuth nitrate pentahydrate ($Bi(NO_3)_3{\cdot}5\ H_2O$), potassium bromide (KBr), hexamethylenetetramine, and D-mannitol (AR) were purchased from Sinopharm Chemical Reagent Co., Ltd. Tris(hydroxymethyl)aminomethane and dopamine hydrochloride were provided by Aladdin Reagent (Shanghai) Co., Ltd. All the regents were used as received without purification.

2.2. Materials synthesis

2.2.1. Preparation of SiO_2 nanospheres

The SiO_2 nanospheres were prepared by the classic Stöber method. Solution A (9 mL of ammonia and 16.5 mL of water) was dissolved in 24.5 mL of ethanol, and solution B (4.5 mL TEOS) was placed in 45.5 mL of ethanol. Solution B was poured into solution A quickly and stirred at 1100 rpm for 2 min and 350 rpm for 2 h. The product was centrifuged, washed with deionized water and ethanol, and dried to obtain the SiO_2 nanospheres.

2.2.2. Preparation of hollow nitrogen-doped carbon spheres (NC)

The SiO_2 nanospheres (0.5 g) was dispersed in the tris(hydroxymethyl)aminomethane buffer solution with a pH of 8.5, and dopamine hydrochloride (0.2 g) was added. After sonication for 5 min, it was stirred at room temperature for 22 h to form a brown-black solution. The solid obtained by centrifugation and washing was heated to 800 °C for 2 h under N_2. The calcined product was etched with 4 M NH_4HF_2 for 24 h to remove the SiO_2 template and obtain NC.

2.2.3. Preparation of $Bi_4O_5Br_2$ nanosheets-loaded hollow nitrogen-doped carbon sphere (BOB@NC) hollow confined electron pump reactor

10 mg of NC, 1.5 mmol hexamethylenetetramine, and 20 mL of the mannitol solution (0.1 M) were added to a 100 mL round-bottom flask and stirred for 15 min to form solution A. 0.3 mmol $Bi(NO_3)_3{\cdot}5\ H_2O$ was dissolved in 10 mL of the mannitol solution (0.1 M) to form solution B, and 0.3 mmol KBr was dissolved in 10 mL of the mannitol solution (0.1 M) to form solution C. Solution B was added dropwise to solution A and stirred for 15 min before solution C was added. After stirring for 30 min, the mixture was placed in a 90 °C oil bath for 6 hours. The product was centrifuged, washed, and dried to obtain the BOB@NC nanoconfined reactor. The preparation steps of the comparative

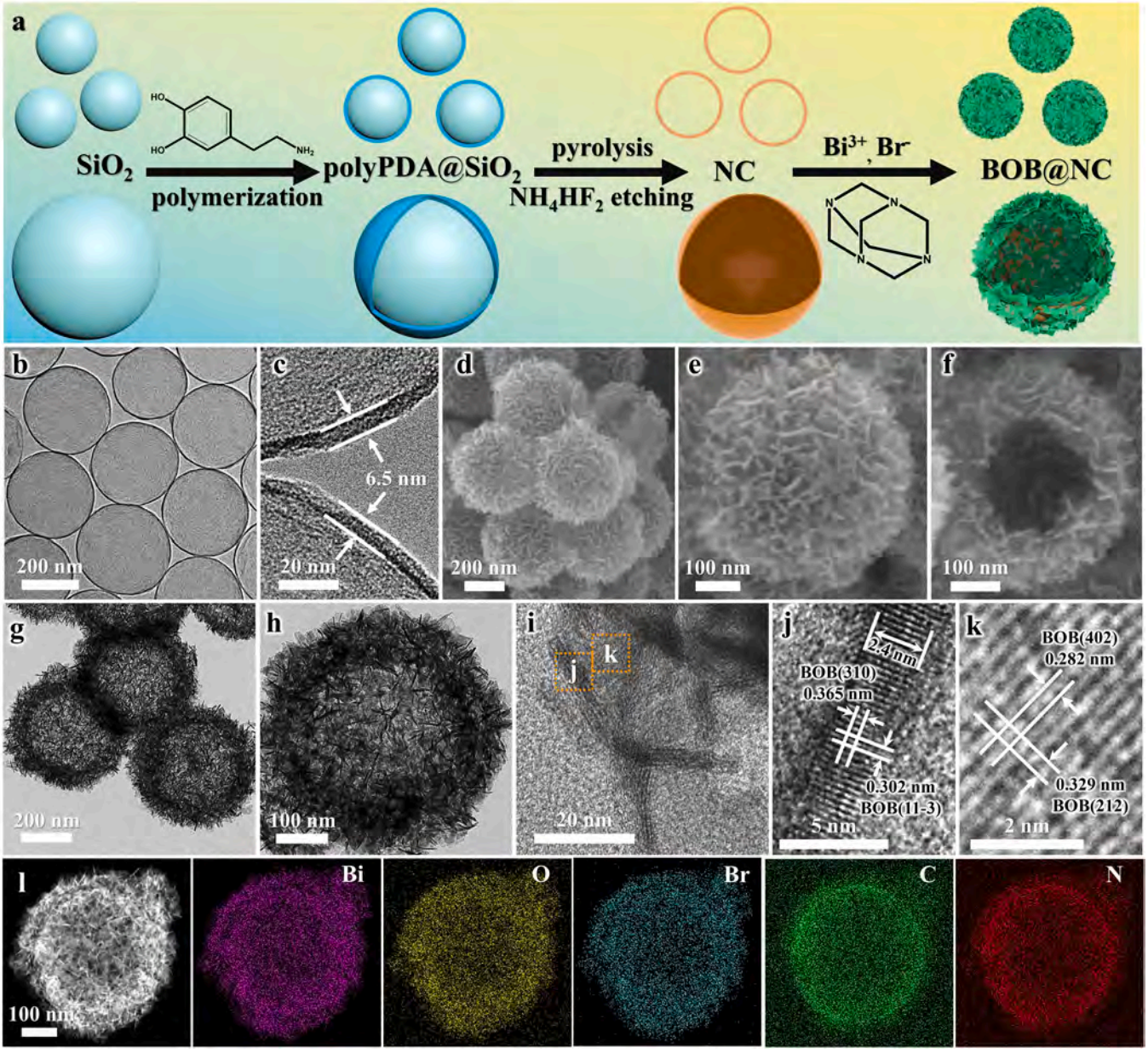

Fig. 1. (a) Schematic illustration of the synthesis of BOB@NC; (b, c) TEM images of NC; (d-f) SEM images, (g-i) TEM images, (j-k), HR-TEM images, and (l) EDS maps of BOB@NC.

materials, BOB@NC-1 and BOB@NC-5, were similar to those of BOB@NC, except that the ratios of NC:$Bi(NO_3)_3{\cdot}5\ H_2O$:KBr in the raw materials were 10 mg : 0.1 mmol : 0.1 mmol and 10 mg : 0.5 mmol : 0.5 mmol, respectively. The preparation steps for the monomer BOB were the same as those of BOB@NC, except that NC was not added.

2.3. Characterization

Powder X-ray diffraction (XRD) was performed on the XRD-6100 (Shimadzu Corporation) and the Raman scattering spectra were obtained on the micro-Raman spectrometer (Renishaw Invia) with a back-scattering geometry and 532 nm laser. The specific surface area and particle size of the samples were derived by the Brunauer-Emmett-Teller (BET) method based on the N_2 adsorption-desorption isotherms (Micromeritics Instrument Corporation, USA). The UV-Vis spectra were acquired by UV-Vis spectrophotometry on the UV-2450 (Shimadzu Corporation). X-ray photoelectron spectroscopy (XPS) was conducted on the PHI5300 with a monochromatic Mg K_α source. The micromorphology of the samples was examined by scanning electron microscopy (SEM) (JEOL JSM-7001 F) and transmission electron microscopy (TEM) (JEOL-JEM-2010). The surface potential of the photocatalysts was studied using Kelvin probe force microscopy (KPFM, MFP-3D-BIO). The photocurrent and electrochemical impedance spectroscopy (EIS) data were collected in the phosphate buffer solution (0.1 M PBS, pH = 7.0), 0.1 M KCl, and 0.1 M KCl containing 5 mM $Fe(CN)_6^{3-}/Fe(CN)_6^{4-}$, respectively on the CHI 760E electrochemical system (CH Instruments Ins.). The *in situ* FTIR spectra were obtained on the diffuse reflectance Fourier transform infrared spectrometer (Thermo Fisher Nicolet iZ10, USA).

The COMSOL multi-physics simulation software was used to simulate the photoinduced semiconductor electric field intensity of BOB-loaded NC. The model was constructed based on the TEM image of BOB@NC, where the BOB model is 20 nm × 20 nm × 2.4 nm, and the NC model is a semicircular structure with a thickness of 6.5 nm. The wavelength of the simulated incident light is 420 nm.

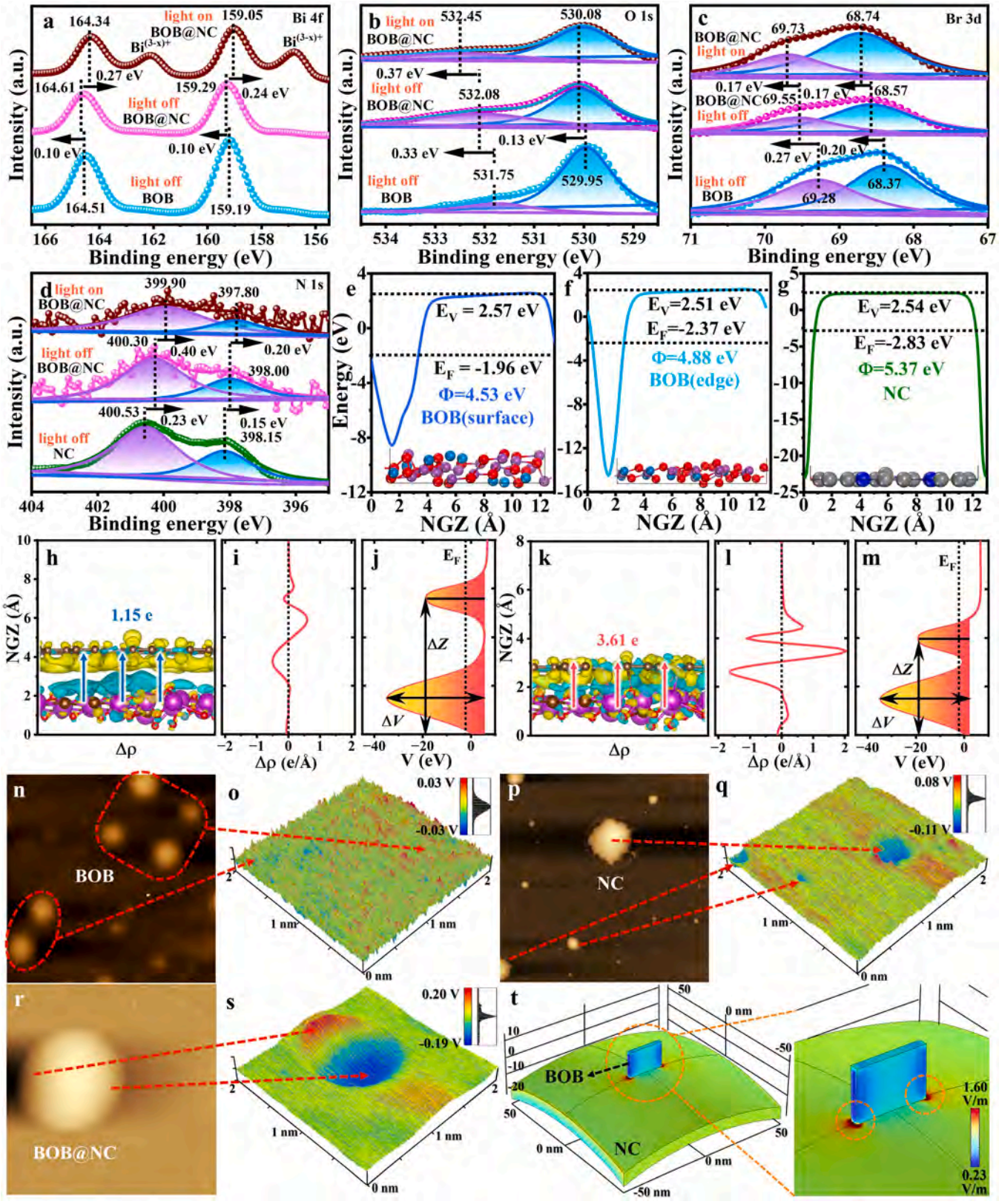

Fig. 2. High-resolution XPS spectra of (a) Bi 4 *f*, (b) O 1 *s*, (c) Br 3*d*, and (d) N 1 *s* of BOB, NC, and BOB@NC; Calculated work functions and structural models of (e) $BOB_{surface}$, (f) BOB_{edge}, and (g) NC. Electronic structures of the BOB@NC models (h-j) without and (k-m) with Bi-C bonds; (h, k) Calculated charge density difference, (i, l) Plane-averaged charge-density difference, and (j, m) Plane-averaged electrostatic potentials along the Z direction; AFM images of (n) BOB, (p) NC, and (r) BOB@NC; KPFM surface potential maps of (o) BOB, (q) NC, and (s) BOB@NC; (t) Spatial distributions of photoinduced electric field of BOB@NC excited by 420 nm light based on COMSOL simulation.

2.4. Photocatalytic CO_2 reduction activity

The catalyst (20 mg) spread on a quartz sample stage was placed in the Pyrex reactor. After deionized water was injected into the Pyrex reactor, it was connected to an online closed gas circulation system for vacuuming (Labsolar-6A, Beijing Perfectlight Technology Co., Ltd.). High-purity CO_2 gas was injected into the reactor. The steps of vacuuming and introducing CO_2 gas were repeated 3 times to ensure that all the air in the reactor was removed. The pressure was adjusted to 80 kPa. The photocatalytic CO_2 reduction assessment was carried out with a 300 W xenon lamp (PLS-SXE300+, Beijing Perfectlight Technology Co., Ltd.) as the light source and gas samples were taken for gas chromatography (Panna (Changzhou) Instruments Co., Ltd.) every hour.

2.5. DFT calculation details

2.5.1. Structure of NC and BOB

The NC model was constructed based on experimental observations and optimized using DFT calculations. In the simulations, the non-periodic boundary condition is employed, and the molecular model of a pristine graphene sheet with 48 carbon atoms was established by using Materials Studio. Nitrogen and hydrogen atom doping in the graphene structure were formed by replacing some carbon atoms from the rings. The BOB was built by considering the most stable surface termination, including Z atomic layers, which is sufficient to capture the interfacial interactions and charge redistribution.

2.5.2. Model construction

The heterostructure was built by aligning the NC and BOB structures based on minimal lattice mismatch to maintain realistic interfacial properties. A vacuum layer of 10 Å was introduced to eliminate spurious interactions in periodic boundary conditions. To find the thermal stable morphology and achieve a conformation with minimum potential energy, energy minimization was performed. Minimum energy conformations were used as the initial status in the subsequent electronic structure simulations. The Visualization for Electronic and Structural Analysis (VESTA, series 3) [35] softwares were used for visualization and plotting.

2.5.3. First-principles calculations

The first-principles calculations were performed with the Vienna Ab initio Simulation Package (VASP) by the projector augmented wave (PAW) method [36,37]. The exchange-functional was treated by the Perdew-Burke-Ernzerhof (PBE) [38] functional, in combination with the DFT-D correction [39]. The calculations were performed in a spin-polarized manner. The cut-off energy of the plane-wave basis was set at 520 eV. A (3 × 3 × 1) Monkhorst-Pack mesh was used for the Brillouin-zone integration to be sampled. The conjugate gradient algorithm was used in the optimization. The convergence threshold was set to 1×10^{-5} eV in the total energy and 0.02 eV/ Å in the force on each atom.

The adsorption energy change (ΔE_{abs}) was determined as follows:

$$\Delta E_{abs} = E_{total} - E_{slab} - E_{mol}$$

where E_{total} is the total energy for the adsorption state, E_{slab} is the energy of the pure surface, and E_{mol} is the energy of the adsorption molecule.

The free energy change (ΔG) for adsorptions was determined as follows:

$$\Delta G = E_{total} - E_{slab} - E_{mol} + \Delta E_{ZPE} - T\Delta S$$

where E_{total} is the total energy for the adsorption state, E_{slab} is the energy of the pure surface, E_{mol} is the energy of the adsorption molecule, ΔE_{ZPE} is the zero-point energy change, and ΔS is the entropy change.

3. Results and discussion

3.1. Synthesis and structural characterization of BOB@NC catalyst

The preparation of the BOB@NC hollow confined electron pump reactor is shown in Fig. 1a. Firstly, monodispersed SiO_2 nanospheres with a diameter of about 300 nm are synthesized to form the template by the Stöber method (Fig. S1) [40]. Polydopamine (polyPDA) with a thickness of about 8 nm is then prepared on the SiO_2 nanospheres (Fig. S2). The polyPDA@SiO_2 precursor is calcined to carbonize polyPDA, and further NH_4HF_2 etching of SiO_2 produces hollow nitrogen-doped carbon spheres (NC) with a diameter of about 300 nm and a wall thickness of about 6.5 nm (Fig. 1b-c). After the NC is introduced to a solution containing Bi^{3+} and Br^-, BOB ultrathin nanosheets are dispersed uniformly on the NC in an oil bath method to form the BOB@NC hollow confined electron pump reactor. As shown in Fig. 1d-h, when the ratio of NC to Bi^{3+}/Br^- is 10 mg:0.3 mmol, BOB nanosheets cover the NC surface completely, and there is no obvious overlap between BOB sheets, thereby allowing the BOB on the BOB@NC surface to fully absorb sunlight and have abundant pores to trap CO_2 gas. Comparative experiments show that when the ratio of NC to Bi^{3+}/Br^- is 10 mg : 0.1 mmol, only a small amount of BOB nanosheets is observed from the NC surface (Fig. S3). When the ratio is 10 mg : 0.5 mmol, BOB nanosheets grow extensively and stack on the NC surface (Fig. S4). If the raw material does not contain NC, the BOB ultrathin nanosheets stack freely and disorderly (Fig. S5). HR-TEM reveals that the thickness of the BOB nanosheets is about 2.4 nm. The lattice fringes of 0.365 and 0.302 nm of BOB(edge) correspond to the (310) and (11−3) planes, respectively (Fig. 1i-j), while those of 0.282 and 0.329 nm of BOB(surface) are associated with the (402) and (212) planes, respectively (Fig. 1k). The EDS maps acquired from BOB@NC reveal that Bi, O, and Br exist mainly in the outer layer of BOB, while N and C are mainly in the inner layer of NC (Fig. 1l). The XRD (Fig. S6), Raman scattering (Fig. S7), and derivation of the BET specific surface area (Fig. S8) confirm that the BOB@NC hollow confined electron pump reactor has a multi-level porous structure.

The electronic structure, band structure, and optical properties of the materials are determined. The chemical composition and chemical states of BOB, NC, and BOB@NC are determined by XPS (Fig. 2a-d). As shown in the high-resolution XPS spectra of Bi 4 *f* (Fig. 2a), two peaks at 159.19 and 164.51 eV are assigned to Bi $4f_{5/2}$ and Bi $4f_{7/2}$, respectively, suggesting that Bi^{3+} exists in BOB [26,41]. In the high-resolution XPS spectra of O 1 *s* (Fig. 2b), the peaks at 529.95 and 531.75 eV correspond to lattice oxygen and oxygen near oxygen vacancies, respectively [42,43]. The peaks at 68.37 and 69.28 eV are ascribed to Br 3*d* of Br^- for BOB (Fig. 2c) [44]. The deconvoluted high-resolution XPS N 1 *s* spectrum reveal two nitrogen species in NC, including pyridinic-N (398.15 eV) and graphitic-N (400.53 eV) (Fig. 2d) [40]. After BOB is prepared on NC, the Bi 4 *f*, O 1 *s*, and Br 3*d* XPS peaks of the BOB@NC nanoconfined reactor shift toward higher energy compared to the BOB monomer, while the N 1*s* XPS peak of BOB@NC shifts toward lower binding energy relative to the NC monomer, indicating interactions between BOB and NC in BOB@NC and some electrons on the surface of BOB are transferred to NC [24,45].

The calculated work functions (Φ) of the exposed crystal faces on BOB(surface) and BOB (edge) are 4.53 and 4.88 eV, respectively, both of which are smaller than that of NC (Φ = 5.37 eV) (Fig. 2e-g). Hence, when BOB nanosheets grow vertically on the NC surface, electrons on the BOB(surface) tend to migrate to BOB(edge), while electrons on BOB (edge) tend to migrate to the NC surface [46,47]. Density-functional theory calculation is performed to analyze the interfacial properties of BOB@NC with and without Bi-C covalent bonds (Fig. 2h-m). The iso-surface of the charge density difference ($\Delta\rho$) is defined as $\Delta\rho = \rho(BOB@NC) - \rho(BOB) - \rho(NC)$, where $\rho(BOB@NC)$, $\rho(BOB)$, and $\rho(NC)$ are the total charge densities of BOB@NC, BOB, and NC, respectively. The calculated differential charge density discloses that the charge

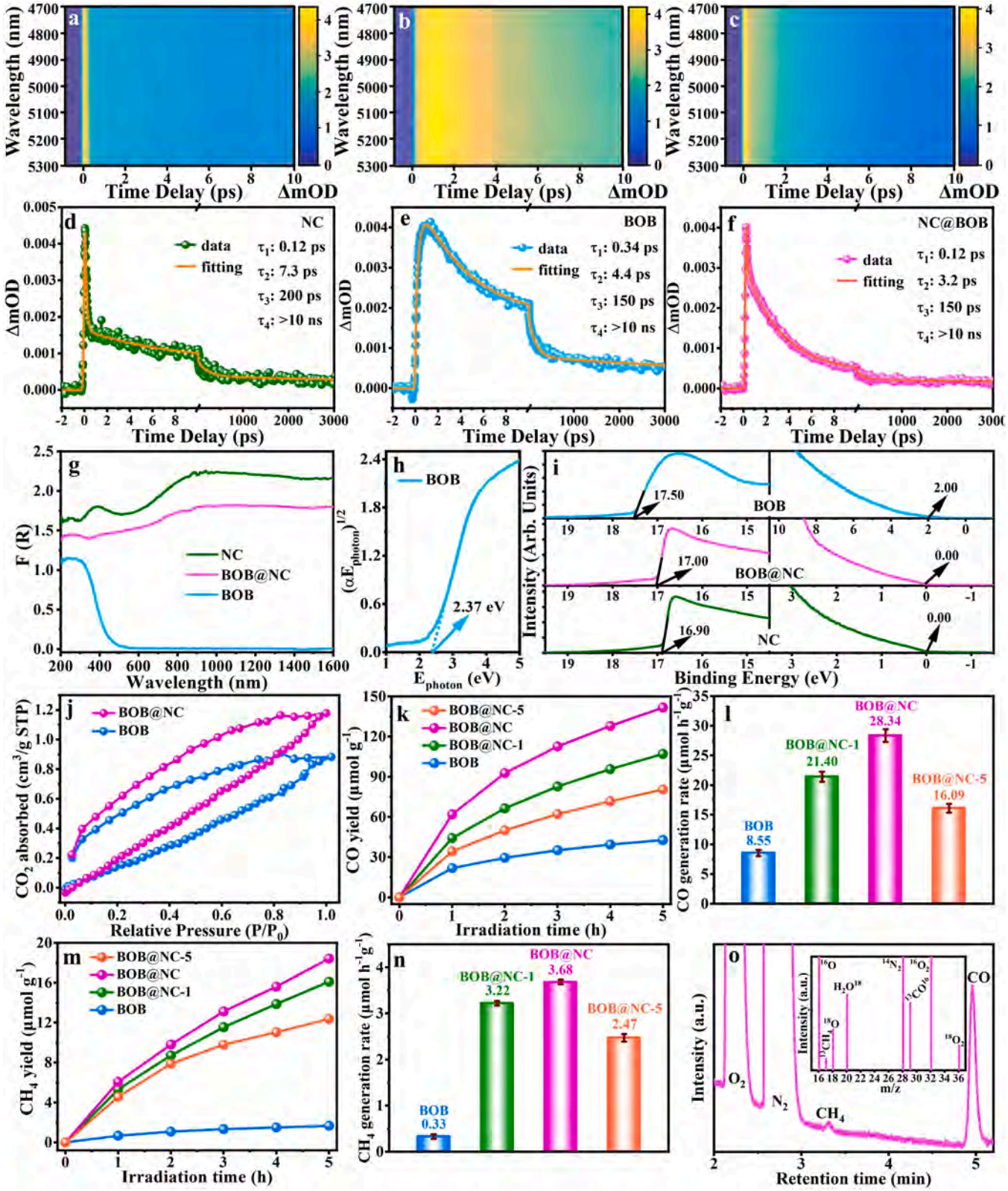

Fig. 3. 3D plots of femtosecond transient absorption spectra of (a) NC, (b) BOB, and (c) BOB@NC for a pumping wavelength of 400 nm; Decay curves of femtosecond transient absorption spectra at 5000 nm of (d) NC, (e) BOB, and (f) BOB@NC; (g) UV–vis diffuse reflection spectra and (i) UPS spectrum of BOB, NC, and BOB@NC; (h) $(\alpha E_{photon})^{1/2}$ vs E_{photon} curves of BOB; (j) CO_2 adsorption-desorption isotherms of BOB and BOB@NC; Photocatalytic (k) CO evolution and (m) CH_4 evolution with time; Average (l) CO and (n) CH_4 production rates of NC, BOB, and BOB@NC; (o) GC-MS spectra of the products after $^{13}CO_2$ and H_2O^{18} photoreduction for BOB@NC.

density is redistributed more abundantly near the interface with Bi-C bonds between BOB and NC (Fig. 2h and k). The number of electrons transferred between BOB and NC (Δq) is determined by the Bader charge according to the formula of $\Delta q(z) = \int_{-\infty}^{z} \Delta\rho(z')dz'$. The results show that when BOB is in close proximity with NC (without Bi-C bonds), BOB tends to transfer electrons to the NC surface [48]. Growing BOB on NC creates Bi-C bonds, and BOB can transfer 3.61e electrons to NC to promote charge transfer. Meanwhile, the average charge density difference in the vacuum layer plane at the interface of BOB@NC with Bi-C bonds shows more obvious redistribution and a stronger built-in electric field (Fig. 2i and l)[49]. The planar electrostatic potential of BOB@NC along the z-axis is studied to explore the interfacial charge transfer limited by the potential energy barrier (Fig. 2j and m). Compared with BOB@NC without Bi-C bonds ($\Delta V = 40.47$ eV, $\Delta Z = 5.60$ Å), BOB@NC with Bi-C bonds exhibit smaller $\Delta V = 36.72$ eV and $\Delta Z = 3.97$ Å, meaning that the electron tunneling barrier is smaller and charge transfer is enhanced [50]. These theoretical results are consistent with the XPS peak shifts observed from the monomer BOB, NC, and BOB@NC.

Kelvin probe force microscopy (KPFM) is used to evaluate the local work functions of BOB, NC, and BOB@NC surfaces and the contact potential difference (CPD) on these materials with the aid of an Au tip as the cantilever (Fig. 2n-s). V_{cpd} is calculated by $V_{cpd} = (\Phi_{tip} - \Phi_{sample})/e$, where Φ_{tip} and Φ_{sample} are the work functions of the tip and sample, respectively. As shown in Fig. 2n-o, the surface potential of BOB does not change significantly, indicating that the work function is similar to that of the Au tip ($\Phi_{Au\ tip} \approx 5.1$ eV), whereas the CPD of NC is as low as -0.11 V and the work function of NC is about 5.21 eV (Fig. 2p-q). The work function trends of monomer BOB and NC assessed by KPFM are similar to those derived by theoretical calculations (Fig. 2e-g). It is worth noting that the CPD of the BOB@NC nanoreactor is between -0.19–0.20 V, and the positive/negative charges are higher than those of the monomer BOB and NC, resulting in significant charge separation (Fig. 2r-s) [51,52]. This is because the Fermi energy levels at the heterojunction are flattened after the growth of BOB on NC, and electrons on BOB with a small figure of merit migrate to NC with a large figure of merit, resulting in the formation of a built-in electric field and a significant surface potential difference. The KPFM results are in line with the XPS and theoretical calculation results.

The aforementioned results provide guidance on the mechanism of interfacial electron transfer in the BOB@NC nanoreactor. The electron migration paths and laws of BOB@NC composites in the photoexcited state are further analyzed. As shown in synchronous illumination XPS spectra (Fig. 2a-d), upon light irradiation, the Bi 4*f* and N 1*s* peaks of BOB@NC shift toward lower binding energy, and two new $Bi^{(3-x)+}$ peaks appear in the Bi 4*f* spectrum [42,53]. The peaks of lattice oxygen of BOB@NC do not change during light illumination, while oxygen near oxygen vacancies decreases significantly (Fig. 2b). Meanwhile, the Br 3*d* peak of BOB@NC shifts toward higher binding energy under light irradiation (Fig. 2c). It is speculated that the electrons of oxygen atoms near oxygen vacancies and Br atoms tend to migrate to Bi atoms during photoexcitation. This is consistent with the densities of states of BOB. That is, electrons in the valence band (VB) of O and Br atoms migrate to the conduction band of Bi atoms (Fig. S9) [54]. The photogenerated electrons in the Bi atom further migrate to the N site in NC through the Bi-C bond. The model of BOB nanosheets grown on NC is designed by the COMSOL multi-physics simulation software (Fig. 2t). Upon 420 nm light irradiation, the junction between BOB and NC shows the maximum electric field for the separation channel of photogenerated electrons [55,56]. In addition, compared with BOB, BOB@NC with a smaller electrochemical impedance is more conducive to the migration of photogenerated electrons (Fig. S10) and shows a higher photocurrent intensity (BOB@NC is 6 times that of BOB) (Fig. S11) and smaller fluorescence intensity (Fig. S12), meaning that BOB@NC generates more photogenerated free electrons.

Femtosecond time-resolved transient absorption spectroscopy (TA) is employed to study the dynamic characteristics and migration paths of photogenerated carriers in the BOB@NC nanoconfined reactor (Fig. 3a-f). During 400 nm pump excitation (light intensity: 68 μJ/cm^2), the 3D plots (wavelength *vs.* time *vs.* intensity) of TA of NC, BOB and BOB@NC exhibit obvious electron relaxation in the infrared region (4700–5300 nm) (Fig. 3a-c). The exponential decay and kinetic properties of photogenerated electrons are investigated by a 5000 nm mid-infrared probe, and the decay curves of the three materials are fitted with four components (Fig. 3d-f), in which τ_1 corresponds to the e-e scattering phenomenon of photogenerated electrons in the material [57,58]. NC and BOB@NC show the same τ_1 ($\tau_{1(NC)} = \tau_{1(BOB@NC)} = 0.12$ ps), which is significantly smaller than that of BOB ($\tau_{1(BOB)} = 0.34$ ps). This indicates that when BOB@NC is excited by light, the photogenerated electrons on BOB move quickly to NC and e-e scattering occurs on the NC surface. τ_2, τ_3, and τ_4 represent the process of photogenerated electrons and holes generating e-h excitons, electrons in the e-h exciton state migrating to the defect state, and defect state electrons relaxing to the VB, respectively [43,59]. The τ_2 and τ_3 values of pure NC ($\tau_{2(NC)} = 7.3$ ps, $\tau_{3(NC)} = 200$ ps) are larger than those of pure BOB ($\tau_{2(BOB)} = 4.4$ ps, $\tau_{3(BOB)} = 150$ ps) because the photogenerated carriers of NC with metallic properties recombine quickly. Since there are fewer free electrons, the time for free electrons to migrate to the exciton state and defect state is longer. In the BOB@NC nanoconfined reactor, a large number of photogenerated electrons migrate from BOB to the NC surface, thereby accelerating the generation of e-h exciton states on the NC surface ($\tau_{2(BOB@NC)} = 3.2$ ps). Meanwhile, more exciton state electrons on the NC surface move to the defect states faster ($\tau_{3(BOB@NC)} = 150$ ps). The rapid electron transfer process on the NC electron pump surface improves the separation efficiency of photogenerated electrons of BOB and concentrates electrons in the defect states of NC. The defect states of NC are mainly composed of N dopants which themselves contain lone pairs of electrons. Therefore, the N site is expected to be an ideal active site for reduction reactions. The rapid directional transfer of photogenerated electrons in the BOB@NC hollow confined electron pump reactor facilitates the effective separation of carriers and increases the local free electron concentration [60,61].

The band structure of the materials is determined by UV–vis diffuse reflectance spectroscopy and ultraviolet photoelectron spectroscopy (UPS) [62]. The UV–vis diffuse reflection spectra show that the maximum light absorption edge of BOB is around 550 nm, while the black NC extends the absorption edge to the infrared region. The light absorption edge of the BOB@NC nanoconfined reactor with BOB on NC also reaches the infrared region (Fig. 3g). According to the $(\alpha E_{photon})^{1/2}$ versus E_{photon} curves of BOB, the bandgap is about 2.37 eV (Fig. 3h). The VB and Fermi levels of BOB and NC are determined by UPS using a monochromatic He I light source ($h\nu = 21.20$ eV) (Fig. 3i). The onset (E_{onset}) and cutoff (E_{cutoff}) energies are 2.00 and 17.50 eV for BOB, 0.00 and 16.90 eV for NC, and 0.00 and 17.00 eV for BOB@NC, respectively. The work function (*vs* vacuum) can be determined by the difference between the photon energy (21.20 eV) and E_{cutoff}. The values of BOB and NC are 3.70 and 4.30 eV, respectively. The trend of the work functions obtained by UPS ($\Phi_{NC} > \Phi_{BOB}$) is consistent with theoretical calculations and KPFM. The energy of the highest electron-occupied orbital, i.e., the VB position, is the sum of the work function and E_{onset}. The E_{onset} value of NC is 0 indicative of the unique metallic properties [63,64]. According to the relationship between the potential of vacuum energy (E_{abs}) and the normal hydrogen electrode (NHE, E•), $E• = -E_{abs} - 4.44$ (at 298 K) [65], the VB of BOB is 1.26 V. The conduction band (CB) position ($E_{CB} = -1.11$ V) of BOB can be obtained by subtracting the bandgap ($E_g = 2.37$ eV) from VB ($E_{VB} = 1.26$ V) (Fig. S13). In the pristine state, BOB exhibits a higher Fermi level than NC. During interfacial contact, electrons move spontaneously from BOB to NC until Fermi level equilibrium is achieved, consequenlty generating a built-in electric field directed from BOB to NC and a corresponding space charge region. During this process, upward band bending on the BOB side suppresses further electron transfer, while the Schottky barrier

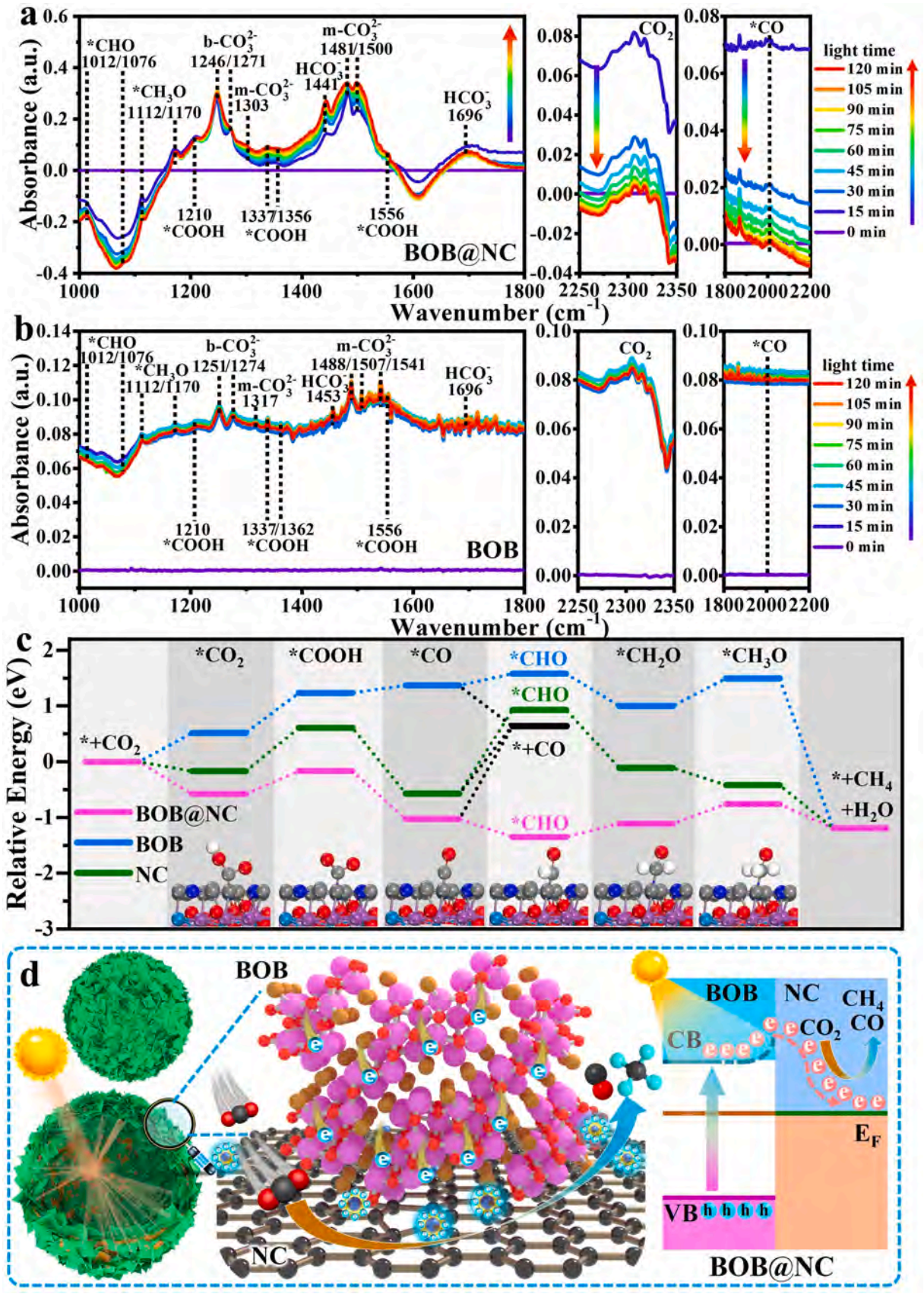

Fig. 4. *In situ* FTIR spectra of (a) BOB@NC and (b) BOB for simulated solar-driven CO_2 reduction; (c) Free energy diagrams of CO_2 photoreduction to CO and CH_4 on BOB and BOB@NC; (d) Schematic illustration of CO_2 conversion on the BOB@NC hollow confined electron pump reactor.

blocks reverse charge migration. Under photoexcitation, valence band electrons in BOB are excited to the conduction band to generate high-energy photogenerated carriers. These electrons overcome the interfacial band bending barrier and migrate directionally to the NC surface to participate in reduction reactions. This charge transfer mechanism aligns with both theoretical simulations of band alignment characteristics and experimental results, thereby validating the effectiveness of heterojunction interface engineering in regulating carrier dynamics.

3.2. Evaluation of photocatalytic CO_2 reduction

In addition to enhancing the migration and separation efficiency of photogenerated carriers for photocatalysis, adsorption of the reactant CO_2 is a key factor in artificial photosynthesis. The CO_2 adsorption-desorption isotherms show that the CO_2 adsorption capacity of BOB@NC (1.18 cm^3/g) is greater than that of BOB (0.88 cm^3/g) at 1 atm (Fig. 3j), indicating the BOB@NC nanoconfined reactor adsorbs more CO_2 molecules[66]. Based on the enhanced photogenerated carrier separation efficiency and CO_2 capacity of BOB@NC, photocatalytic CO_2 reduction is monitored. As shown in Fig. 3k-n, the BOB@NC nanoconfined reactor delivers the best photocatalytic performance for CO_2 reduction to CO and CH_4. After illumination for 5 hours, the CO and CH_4 yields of BOB@NC are 28.34 and 3.68 umol h^{-1} g^{-1}, respectively, which are 3.31 and 11.15 times better that those of BOB, and more importantly, these properties are better than those of previously reported photocatalytic CO_2 reduction materials (Table S1).

The stability of BOB@NC in photocatalytic CO_2 reduction is assessed, and it is found that the production of CO and CH_4 continues to rise during long-term illumination (Fig. S14). The XRD (Fig. S15) and TEM (Fig. S16) results of BOB@NC after the stability test reveal no significant changes in the crystal structure or morphology, confirming both the good activity and structural stability of BOB@NC. The photocatalytic properties of BOB@NC-1 and BOB@NC-5 are inferior to those of BOB@NC because there is not enough BOB on the NC surface for BOB@NC-1, while a large amount of BOB does not grow on the NC surface of BOB@NC-5, rendering them not conducive to directional migration and separation of photogenerated carriers. In order to determine the carbon source of the CO_2 photoreduction products, the photocatalytic reaction is monitored using isotope-labeled $^{13}CO_2$ and H_2O^{18}. As shown in Fig. 3o, the peaks at 2.2, 2.7, 3.3, and 4.9 min in the GC-MS spectra correspond to O_2, N_2, CH_4, and CO, respectively. The signals at 17, 29, and 36 in the mass spectrum correspond to $^{13}CH_4$, $^{13}CO^{16}$, and $^{18}O_2$, respectively, confirming that the ^{13}CO and $^{13}CH_4$ products are derived from $^{13}CO_2$, and H_2O^{18} is oxidized to generate $^{18}O_2$ during photocatalytic CO_2 reduction [67,68].

3.3. Proposed mechanisms for photocatalytic CO_2 hydrogenation reduction

The photocatalytic CO_2 conversion mechanism is explored by *in situ* FTIR and theoretical calculations. As shown in Fig. 4a, during extended illumination, the peak intensity of $*CO_2$ at 2250–2350 cm^{-1} and *CO at 1800–2200 cm^{-1} decrease significantly and rapidly, indicating that CO_2 adsorb rapidly and is activated and hydrogenated to generate *CO intermediates on BOB@NC [42,69]. Other key intermediates such as *COOH (1210, 1337, 1356, and 1556 cm^{-1}), *CHO (1012 and 1076 cm^{-1}), and $*CH_3O$ (1112 and 1170 cm^{-1}) are observed [70,71]. Compared to photocatalytic CO_2 reduction on BOB@NC, the changes of the $*CO_2$ and *CO absorption peaks of BOB are not obvious, and the intensity of the peaks of the other intermediate products is very weak (Fig. 4b), indicating that the ability of adsorption-activation-conversion of CO_2 molecules on the surface of BOB monomer is relatively depressed, giving rise to low CO and CH_4 yields. The free energy barriers are calculated based on the intermediate products detected by *in situ* infrared spectroscopy. As shown in Fig. 4c, the N site on NC and BOB@NC adsorbs CO_2 spontaneously, while the adsorption of CO_2 on BOB is endothermic. Furthermore, in the CO_2 reduction process, the rate-determining steps of both BOB@NC and BOB are $*CO_2 \rightarrow *COOH$, and the rate-determining step energy barrier of BOB@NC is 0.41 eV, which is much smaller than 0.72 eV of BOB. The rate-determining step in CO_2 reduction on NC is the desorption of *CO (1.21 eV). Meanwhile, the conversion of *COOH to *CO is exothermic at the N site of NC on BOB@NC, while BOB continues to undergo an endothermic process. On the BOB surface, *CO desorption and hydrogenation reactions are exothermic and endothermic, respectively, so CO is easier to desorb from the BOB surface, whereas hydrogenation is more difficult. This results in a low CH_4 yield. On the N site of pure NC, the energy barrier for the hydrogenation of *CO to *CHO is higher than that for the desorption of *CO. At the N site on BOB@NC, desorption of *CO needs to overcome a high energy barrier, while the $*CO \rightarrow *CHO$ hydrogenation reaction is exothermic and can proceed spontaneously to continue to receive electrons for reduction to CH_4. The spectroscopic results, in conjunction with band structure and theoretical calculations, corroborate that the N site of NC on BOB@NC based on the interaction between BOB and NC serves as both an enrichment center for photogenerated electrons and an active site for CO_2 adsorption-activation-hydrogenation, consequently boosting the CO_2 photocatalytic reduction performance.

Based on the experimental investigation and theoretical simulation, Fig. 4d illustrates the photocatalytic CO_2 reduction mechanism of the BOB@NC hollow confined electron pump reactor. Firstly, the unique hollow porous structure of BOB@NC enables multiple reflections and diffractions of the incident light in the cavity to improve light utilization. Secondly, during photoexcitation, valence band electrons in BOB are excited to the conduction band to generate high-energy photogenerated carriers. These electrons overcome the interfacial band bending barrier (Schottky barrier) and move directionally to NC. The photogenerated electrons on the NC surface undergo e-h exciton state formation quickly and migrate to the N-induced defect state of NC, thereby effectively separating the photogenerated electrons from BOB and enriching the photogenerated electrons at the nitrogen sites. Thirdly, the N sites on the NC surface adsorb CO_2 spontaneously for *CO hydrogenation while reducing the generation of *COOH intermediates in the rate-determining step. Therefore, compared with the BOB monomer, the BOB@NC nanoconfined reactor delivers significantly better performance in the photocatalytic generation of CO and CH_4.

4. Conclusion

The BOB@NC confined electron pump reactor is designed and constructed by fabricating ultrathin BOB nanosheets uniformly on the NC surface. BOB@NC exhibits improved light absorption and promoted migration of photogenerated electrons from BOB to the NC electron pump surface through the built-in electric field and Bi-C bridging bond. The photogenerated electrons undergo rapid e-h exciton state generation and transfer to defect states on the NC surface, achieving directional migration and effective separation of photogenerated electrons. The nitrogen dopant in NC acts as an enrichment center for photogenerated electrons and also an active site for CO_2 adsorption-activation-hydrogenation, thereby effectively reducing the barrier of the rate-determining step of the reaction and spontaneously inducing hydrogenation of *CO intermediates for the generation of CH_4. The BOB@NC nanoconfined reactor reveals a novel strategy for the design of efficient artificial photosynthesis catalysts.

Declaration of Competing Interest

The authors declare that they have no known competing financial interests or personal relationships that could have appeared to influence the work reported in this paper.

Acknowledgements

This work was financially supported by the National Natural Science Foundation of China (Nos. 22308300, 22138011, 22108106), Natural Science Foundation of Jiangsu Province (BK20220598), City University of Hong Kong Donation Research Grants (DON-RMG Nos. 9229021 and 9220061). Key Laboratory of Electrochemical Energy Storage and Energy Conversion of Hainan Province (KFKT2024005). The authors thank Prof. Ziran Chen of Sichuan Vocational and Technical College for providing access to the Vienna ab-initio simulation package.

Appendix A. Supporting information

Supplementary data associated with this article can be found in the online version at doi:10.1016/j.apcatb.2025.125394.

Data availability

Data will be made available on request.

References

[1] S. Xu, E.A. Carter, Theoretical insights into heterogeneous (photo)electrochemical CO_2 reduction, Chem. Rev. 119 (2019) 6631–6669.
[2] Y. Tao, J. Guan, J. Zhang, S. Hu, R. Ma, H. Zheng, J. Gong, Z. Zhuang, S. Liu, H. Ou, D. Wang, Y. Xiong, Ruthenium single atomic sites surrounding the support pit with exceptional photocatalytic activity, Angew. Chem. Int Ed. 63 (2024) e202400625.
[3] J.O. Olowoyo, V.S. Gharahshiran, Y. Zeng, Y. Zhao, Y. Zheng, Atomic/molecular layer deposition strategies for enhanced CO_2 capture, utilisation and storage materials, Chem. Soc. Rev. 53 (2024) 5428–5488.
[4] X. Li, J. Yu, M. Jaroniec, X. Chen, Cocatalysts for selective photoreduction of CO_2 into solar fuels, Chem. Rev. 119 (2019) 3962–4179.
[5] Z. Jiang, X. Xu, Y. Ma, H.S. Cho, D. Ding, C. Wang, J. Wu, P. Oleynikov, M. Jia, J. Cheng, Y. Zhou, O. Terasaki, T. Peng, L. Zan, H. Deng, Filling metal-organic framework mesopores with TiO_2 for CO_2 photoreduction, Nature 586 (2020) 549–554.
[6] Y. Zhang, Y. Zhou, M.M. Li, J. Di, Surface site design in photocatalytic carbon conversion applications, Coordin. Chem. Rev. 529 (2025) 216459.
[7] Y. Wu, Q. Hu, Q. Chen, X. Jiao, Y. Xie, Fundamentals and challenges of engineering charge polarized active sites for CO_2 photoreduction toward C_2 products, Acc. Chem. Res. 56 (2023) 2500–2513.
[8] T.F. Qahtan, T.O. Owolabi, O.E. Olubi, A. Hezam, Emerging tandem S-scheme heterojunction photocatalysts, Coord. Chem. Rev. 514 (2024) 215839.
[9] B. Pan, Y. Wu, B. Rhimi, J. Qin, Y. Huang, M. Yuan, C. Wang, Oxygen-doping of $ZnIn_2S_4$ nanosheets towards boosted photocatalytic CO_2 reduction, J. Energy Chem. 57 (2021) 1–9.
[10] B. Wang, H. Chen, W. Zhang, H. Liu, Z. Zheng, F. Huang, J. Liu, G. Liu, X. Yan, Y. X. Weng, H. Li, Y. She, P.K. Chu, J. Xia, Semimetallic bismuthene with edge-rich dangling bonds: broad-spectrum-driven and edge-confined electron enhancement boosting CO_2 hydrogenation reduction, Adv. Mater. 36 (2024) 2312676.
[11] J.L. Ortiz-Quiñonez, U. Pal, Interface engineered metal oxide heterojunction nanostructures in photocatalytic CO_2 reduction: progress and prospects, Coord. Chem. Rev. 516 (2024) 215967.
[12] W. Zhang, A.R. Mohamed, W.J. Ong, Z-scheme photocatalytic systems for carbon dioxide reduction: where are we now? Angew. Chem. Int. Ed. 59 (2020) 22894–22915.
[13] S. Roy, A. Joseph, X. Zhang, S. Bhattacharyya, A.B. Puthirath, A. Biswas, C. S. Tiwary, R. Vajtai, P.M. Ajayan, Engineered two-dimensional transition metal dichalcogenides for energy conversion and storage, Chem. Rev. 124 (2024) 9376–9456.
[14] P. Zhang, X.W.D. Lou, Design of heterostructured hollow photocatalysts for solar-to-chemical energy conversion, Adv. Mater. 31 (2019) 1900281.
[15] W. Pan, Z. Wei, Y. Su, Y. Lian, Z. Zheng, H. Yuan, Y. Qin, X. Xie, Q. Bai, Z. Jiao, W. Hua, J. Chen, W. Yang, Z. Deng, Y. Peng, Hydroxylated metal–organic-layer nanocages anchoring single atomic cobalt sites for robust photocatalytic CO_2 reduction, Nano Res. 17 (2023) 2410–2419.
[16] D. Zheng, X.N. Cao, X. Wang, Precise formation of a hollow carbon nitride structure with a janus surface to promote water splitting by photoredox catalysis, Angew. Chem. Int. Ed. 55 (2016) 11512–11516.
[17] P. Zhang, S. Wang, B.Y. Guan, X.W. Lou, Fabrication of CdS hierarchical multi-cavity hollow particles for efficient visible light CO_2 reduction, Energ. Environ. Sci. 12 (2019) 164–168.
[18] S. Das, J. Perez-Ramirez, J. Gong, N. Dewangan, K. Hidajat, B.C. Gates, S. Kawi, Core-shell structured catalysts for thermocatalytic, photocatalytic, and electrocatalytic conversion of CO_2, Chem. Soc. Rev. 49 (2020) 2937–3004.
[19] Y. Kuang, H. Li, Metal@hollow carbon sphere nanoreactors for sustainable biomass and CO_2 valorization, J. Mater. Chem. A 10 (2022) 7557–7603.
[20] X.W. Zhang, P. Wang, X.Y. Lv, X.Y. Niu, X.Y. Lin, S.X. Zhong, D.M. Wang, H.J. Lin, J.R. Chen, S. Bai, Stacking engineering of semiconductor heterojunctions on hollow carbon spheres for boosting photocatalytic CO_2 reduction, ACS Catal. 12 (2022) 2569–2580.
[21] C. Bie, B. Zhu, F. Xu, L. Zhang, J. Yu, In situ grown monolayer N-doped graphene on CdS hollow spheres with seamless contact for photocatalytic CO_2 reduction, Adv. Mater. 31 (2019) e1902868.
[22] C. Cheng, D. Chen, N. Li, Q. Xu, H. Li, J. He, J. Lu, $ZnIn_2S_4$ grown on nitrogen-doped hollow carbon spheres: an advanced catalyst for Cr(VI) reduction, J. Hazard Mater. 391 (2020) 122205.
[23] L. Wang, B. Zhu, B. Cheng, J. Zhang, L. Zhang, J. Yu, In-situ preparation of TiO_2/N-doped graphene hollow sphere photocatalyst with enhanced photocatalytic CO_2 reduction performance, Chin. J. Catal. 42 (2021) 1648–1658.
[24] B. Wang, J.Z. Zhao, H.L. Chen, Y.X. Weng, H. Tang, Z.R. Chen, W.S. Zhu, Y.B. She, J.X. Xia, H.M. Li, Unique Z-scheme carbonized polymer dots/$Bi_4O_5Br_2$ hybrids for efficiently boosting photocatalytic CO_2 reduction, Appl. Catal. B-Environ. 293 (2021) 120182.
[25] A. Chawla, A. Sudhaik, Sonu, P. Raizada, T. Ahamad, Q. Van Le, V. Nguyen, S. Thakur, A.K. Mishra, R. Selvasembian, P. Singh, Bi-rich BixOyBrz-based photocatalysts for energy conversion and environmental remediation: a review, Coord. Chem. Rev. 491 (2023) 215246.
[26] X. Dong, Z. Cui, X. Shi, P. Yan, Z. Wang, A.C. Co, F. Dong, Insights into dynamic surface bromide sites in $Bi_4O_5Br_2$ for sustainable N_2 photofixation, Angew. Chem. Int. Ed. 61 (2022) e202200937.
[27] C.Y. Wang, C. Hu, F. Chen, H.T. Li, Y.H. Zhang, T.Y. Ma, H.W. Huang, Polar layered bismuth-rich oxyhalide piezoelectrics $Bi_4O_5X_2$ (X=Br, I): efficient piezocatalytic pure water splitting and interlayer anion-dependent activity, Adv. Funct. Mater. 33 (2023) 2301144.
[28] X.S. Zhao, Y.Y. You, S.B. Huang, Y.X. Wu, Y.Y. Ma, G. Zhang, Z.H. Zhang, Z-scheme photocatalytic production of hydrogen peroxide over $Bi_4O_5Br_2$/g-C_3N_4 heterostructure under visible light, Appl. Catal. B-Environ. 278 (2020) 119251.
[29] B. Hao, Y. Ahmadi, J. Szulejko, T. Zhang, Z. Lu, K.-H. Kim, The design and fabrication of TiO_2/$Bi_4O_5Br_2$ step-scheme heterojunctions for the photodegradation of gaseous hydrogen sulfide: DFT calculation, kinetics, pathways, and mechanisms, Chin. J. Catal. 68 (2025) 282–299.
[30] H. Wang, Z. Chen, Y. Shang, C. Lv, X. Zhang, F. Li, Q. Huang, X. Liu, W. Liu, L. Zhao, L. Ye, H. Xie, X. Jin, Boosting carrier separation on a BiOBr/$Bi_4O_5Br_2$ direct Z-scheme heterojunction for superior photocatalytic nitrogen fixation, ACS Catal. 14 (2024) 5779–5787.
[31] M. Zha, L. Ai, R. Sheng, C. Tan, Y. Li, N. Guo, M. Xu, D. Jia, L. Wang, Engineering Dual-defective 0D/2D VN-CNQDs/VBi-$Bi_4O_5Br_2$ S-scheme heterostructure for boosting CO_2 photoreduction in air, Small 21 (2024) 2407839.
[32] Q. Luo, X. Deng, T. Zhao, S.-F. Yin, P. Chen, Tailored dynamic Seesaw configuration of heterojunctions to enhance piezo-photocatalytic overall nitrogen fixation, Nano Lett. 25 (2025) 2493–2501.
[33] X. Wang, B. Hu, Y. Li, Z. Yang, G. Zhang, Dipole moment regulation by Ni doping ultrathin $Bi_4O_5Br_2$ for enhancing internal electric field toward efficient photocatalytic conversion of CO_2 to CO, Chin. J. Catal. 66 (2024) 257–267.
[34] H. Tian, Y. Song, R. Zhang, Q. Wang, Y. Ning, B. Liu, Lattice distortion and electronic structure dual engineering of $Bi_4O_5Br_2$ nanosheets for enhanced photocatalytic activity, Chem. Eng. J. 508 (2025) 161000.
[35] K. Momma, F. Izumi, *VESTA3* for three-dimensional visualization of crystal, volumetric and morphology data, J. Appl. Crystallogr. 44 (2011) 1272–1276.
[36] G. Kresse, D. Joubert, From ultrasoft pseudopotentials to the projector augmented-wave method, Phys. Rev. B 59 (1999) 1758–1775.
[37] J.P. Perdew, K. Burke, M. Ernzerhof, Generalized gradient approximation made simple, Phys. Rev. Lett. 77 (1996) 3865–3868.
[38] P.E Blöchl, Projector augmented-wave method, Phys. Rev. B 50 (1994) 17953–17979.
[39] S. Grimme, J. Antony, S. Ehrlich, H. Krieg, A consistent and accurateab initioparametrization of density functional dispersion correction (DFT-D) for the 94 elements H-Pu, J. Chem. Phys. 132 (2010) 154104.
[40] B. Wang, Y. Ye, L. Xu, Y. Quan, W. Wei, W. Zhu, H. Li, J. Xia, Space-confined yolk-shell construction of Fe_3O_4 nanoparticles inside N-doped hollow mesoporous carbon spheres as bifunctional electrocatalysts for long-term rechargeable zinc–air batteries, Adv. Funct. Mater. 30 (2020) 2005834.
[41] G. Liu, L. Li, B. Wang, N. Shan, J. Dong, M. Ji, W. Zhu, P.K. Chu, J. Xia, H. Li, Construction of Bi nanoparticles loaded BiOCl nanosheets ohmic junction for photocatalytic CO_2 reduction, Acta Phys. -Chim. Sin. 40 (2024) 2306041.
[42] B. Wang, W. Zhang, G.P. Liu, H.L. Chen, Y.X. Weng, H.M. Li, P.K. Chu, J.X. Xia, Excited electron-Rich $Bi^{(3-x)+}$ sites: a quantum well-like structure for highly-promoted selective photocatalytic CO_2 reduction performance, Adv. Funct. Mater. 32 (2022) 2202885.
[43] H. Wang, D. Yong, S. Chen, S. Jiang, X. Zhang, W. Shao, Q. Zhang, W. Yan, B. Pan, Y. Xie, Oxygen vacancy-mediated exciton dissociation in BiOBr for boosting charge-carrier-involved molecular oxygen activation, J. Am. Chem. Soc. 140 (2018) 1760–1766.
[44] J. Dong, S. Ji, Y. Zhang, M, Ji, B. Wang, Y. Li, Z. Chen, J. Xia, H. Li, Construction of Z-Scheme MnO_2/BiOBr Heterojunction for Photocatalytic Ciprofloxacin Removal and CO_2 Reduction, Acta Phys. -Chim. Sin. 39 (2023) 2212011.
[45] Y. Jiang, J.F. Liao, H.-Y. Chen, H.-H. Zhang, J.Y. Li, X.D. Wang, D.B. Kuang, All-solid-state Z-scheme α-Fe_2O_3/amine-RGO/$CsPbBr_3$ hybrids for visible-light-driven photocatalytic CO_2 reduction, Chem 6 (2020) 766–780.
[46] B. Wang, X. Zhu, F. Huang, Y. Quan, G. Liu, X. Zhang, F. Xiong, C. Huang, M. Ji, H. Li, P.K. Chu, J. Xia, Porous edge confinement: high carrier potential and low activation energy barrier synergistically boosting the efficiency of selective photocatalytic CO_2 conversion, Appl. Catal. B-Environ. 325 (2023) 122304.

[47] J. Dong, J. Zhao, X. Yan, L. Li, G. Liu, M. Ji, B. Wang, Y. She, H. Li, J. Xia, Construction of carbonized polymer dots/potassium doped carbon nitride nanosheets Van der Waals heterojunction by ball milling method for facilitating photocatalytic CO_2 reduction performance in pure water, Appl. Catal. B-Environ. 351 (2024) 123993.
[48] J.J. Liu, Origin of high photocatalytic efficiency in monolayer g-C_3N_4/CdS heterostructure: a hybrid DFT study, J. Phys. Chem. C 119 (2015) 28417–28423.
[49] X. Zhu, Z. Wang, K. Zhong, Q. Li, P. Ding, Z. Feng, J. Yang, Y. Du, Y. Song, Y. Hua, J. Yuan, Y. She, H. Li, H. Xu, Mo-O-bi bonds as interfacial electron transport bridges to fuel CO_2 photoreduction via in-situ reconstruction of black Bi_2MoO_6/BiO_{2-x} heterojunction, Chem. Eng. J. 429 (2022) 132204.
[50] Y.J. Yuan, Z.K. Shen, S.X. Song, J. Guan, L. Bao, L. Pei, Y.B. Su, S.T. Wu, W.F. Bai, Z.T. Yu, Z.G. Ji, Z.G. Zou, Co-P bonds as atomic-level charge transfer channel to boost photocatalytic H_2 production of Co_2P/black phosphorus nanosheets photocatalyst, ACS Catal. 9 (2019) 7801–7807.
[51] X. Li, H.R. Long, J. Zhong, F. Ding, W. Li, Z.C. Zhang, R. Song, W. Huang, J. Y. Liang, J.L. Liu, R.X. Wu, B. Li, B. Zhao, X.D. Yang, Z.W. Zhang, Y. Liu, Z.M. Wei, J. Li, X.D. Duan, Two-dimensional metallic alloy contacts with composition-tunable work functions, Nat. Electron 6 (2023) 842–851.
[52] S.K. Ravi, W. Sun, D.K. Nandakumar, Y. Zhang, S.C. Tan, Optical manipulation of work function contrasts on metal thin films, Sci. Adv. 4 (2018) eaao6050.
[53] W. Yan, Y. Zhang, Y. Bi, Subnanometric bismuth clusters confined in pyrochlore-$Bi_2Sn_2O_7$ enable remarkable CO_2 photoreduction, Angew. Chem. Int. Ed. 63 (2024) e202316459.
[54] Y.J. Zhang, Z.F. Xu, Q. Wang, W.C. Hao, X. Zhai, X. Fei, X.J. Huang, Y.P. Bi, Unveiling the activity origin of ultrathin BiOCl nanosheets for photocatalytic CO_2 reduction, Appl. Catal. B-Environ. 299 (2021) 120679.
[55] S. Yue, L. Chen, M. Zhang, Z. Liu, T. Chen, M. Xie, Z. Cao, W. Han, Electrostatic field enhanced photocatalytic CO_2 conversion on $BiVO_4$ nanowires, Nano-Micro Lett. 14 (2021) 15.
[56] Q. Liu, F.Q. Zhan, H. Luo, D. Zhai, Z.D. Xiao, Q.W. Sun, Q.Y. Yi, Y. Yang, D. Zhang, Mechanism of interface engineering for ultrahigh piezo-photoelectric catalytic coupling effect of $BaTiO_3$@TiO_2 microflowers, Appl. Catal. B-Environ. 318 (2022) 121817.
[57] A.M. Brown, R. Sundararaman, P. Narang, A.M. Schwartzberg, W.A. Goddard, H. A. Atwater, Experimental and Ab initio ultrafast carrier dynamics in plasmonic nanoparticles, Phys. Rev. Lett. 118 (2017) 087401.
[58] M. Perner, P. Bost, U. Lemmer, G. vonPlessen, J. Feldmann, U. Becker, M. Mennig, M. Schmitt, H. Schmidt, Optically induced damping of the surface plasmon resonance in gold colloids, Phys. Rev. Lett. 78 (1997) 2192–2195.
[59] W. Bi, X. Li, L. Zhang, T. Jin, L. Zhang, Q. Zhang, Y. Luo, C. Wu, Y. Xie, Molecular co-catalyst accelerating hole transfer for enhanced photocatalytic H_2 evolution, Nat. Commun. 6 (2015) 8647.
[60] K. Zheng, M. Wu, J. Zhu, W. Zhang, S. Liu, X. Zhang, Y. Wu, L. Li, B. Li, W. Liu, J. Hu, C. Liu, J. Zhu, Y. Pan, M. Zhou, Y. Sun, Y. Xie, Breaking the activity-selectivity trade-off for CH_4-to-C_2H_6 photoconversion, J. Am. Chem. Soc. 146 (2024) 12233–12242.
[61] Y. Zhang, T. Wei, D. Ding, K. Wang, J. Di, J. Tseng, Y. She, M.M. Li, J. Xia, H. Li, Aggregation-Induced Equidistant Dual Pt Atom Pairs for Effective CO_2 Photoreduction to C_2H_4, ACS Catal 15 (2025) 5614–5622.
[62] B. Pan, Y. Lv, Y. Dong, J. Qin, C. Wang, Hydrochar-supported $NiFe_2O_4$ nanosheets with a tailored microstructure for enhanced CO_2 photoreduction to syngas, Inorg. Chem. 63 (2024) 2148–2156.
[63] N. Koch, A. Elschner, J.P. Rabe, R.L. Johnson, Work function independent hole-injection barriers between pentacene and conducting polymers, Adv. Mater. 17 (2005) 330.
[64] F.Y. Zhang, C. Klein, E. Longhi, S. Barlow, S.R. Marder, G. Sarusi, A. Kahn, Molecular-reductant-induced control of a graphene-organic interface for electron injection, Chem. Mater. 31 (2019) 6624–6632.
[65] J. Liu, Y. Liu, N. Liu, Y. Han, X. Zhang, H. Huang, Y. Lifshitz, S.T. Lee, J. Zhong, Z. Kang, Water splitting. Metal-free efficient photocatalyst for stable visible water splitting via a two-electron pathway, Science 347 (2015) 970–974.
[66] M. Zhou, H. Wang, R. Liu, Z. Liu, X. Xiao, W. Li, C. Gao, Z. Lu, Z. Jiang, W. Shi, Y. Xiong, Construction of frustrated lewis pairs in poly(heptazine imide) nanosheets via hydrogen bonds for boosting CO_2 photoreduction, Angew. Chem. Int. Ed. 63 (2024) e202407468.
[67] S. Wang, B. Jiang, J. Henzie, F. Xu, C. Liu, X. Meng, S. Zou, H. Song, Y. Pan, H. Li, J. Yu, H. Chen, J. Ye, Designing reliable and accurate isotope-tracer experiments for CO_2 photoreduction, Nat. Commun. 14 (2023) 2534.
[68] N. Wang, S. Cheong, D.E. Yoon, P. Lu, H. Lee, Y.K. Lee, Y.S. Park, D.C. Lee, Efficient, selective CO_2 photoreduction enabled by facet-resolved redox-active sites on colloidal CdS nanosheets, J. Am. Chem. Soc. 144 (2022) 16974–16983.
[69] J. Szanyi, J.H. Kwak, Dissecting the steps of CO_2 reduction: 1. The interaction of CO and CO_2 with gamma-Al_2O_3: an in situ FTIR study, Phys. Chem. Chem. Phys. 16 (2014) 15117–15125.
[70] G. Liu, L. Li, B. Wang, J. Yang, J. Dong, N. Shan, W. Zhu, J. Xia, H. Li, Oxygen vacancies-tuned BiOBr nanosheets for accelerating CO_2 and Cr(VI) photoreduction, Appl. Surf. Sci. 660 (2024) 159924.
[71] S. Karmakar, S. Barman, F.A. Rahimi, D. Rambabu, S. Nath, T.K. Maji, Confining charge-transfer complex in a metal-organic framework for photocatalytic CO_2 reduction in water, Nat. Commun. 14 (2023) 4508.

Supporting Information

Epitaxial $Bi_4O_5Br_2$ nanosheets on hollow carbon spheres for confined electron pump reactor and enhanced photocatalytic CO_2 hydrogenation reduction

Bin Wang,[a,b,c] Hailong Chen,[d] Fangcheng Huang,[f] Jinyuan Liu,[a,b] Gaopeng Liu,[a] Yu-Xiang Weng,[d] Yuanbin She,[e] Xingwang Zhu,[c,*] Huaming Li,[a] Jiexiang Xia,[a,*] Paul K. Chu[b,*]

[a] School of Chemistry and Chemical Engineering, Institute for Energy Research, Jiangsu University, 301 Xuefu Road, Zhenjiang 212013, P. R. China

[b] Department of Physics, Department of Materials Science and Engineering, and Department of Biomedical Engineering, City University of Hong Kong, Kowloon, Hong Kong 999077, China

c Institute of Technology for Carbon Neutralization, College of Environmental Science and Engineering, Yangzhou University, Yangzhou 225009, China

[d] Beijing National Laboratory for Condensed Matter Physics, CAS Key Laboratory of Soft Matter Physics, Institute of Physics, Chinese Academy of Sciences, Beijing 100190, P. R. China

[e] College of Chemical Engineering, Zhejiang University of Technology, Hangzhou, Zhejiang 310014, P. R. China

[f] Department of Information Engineering, Electronics, and Telecommunications, Sapienza University of Rome, Piazzale Aldo Moro 5, Roma 00185, Italy

* Corresponding authors: zxw@yzu.edu.cn (X.Z.); xjx@ujs.edu.cn (J.X.); paul.chu@cityu.edu.hk (P.K.C.)

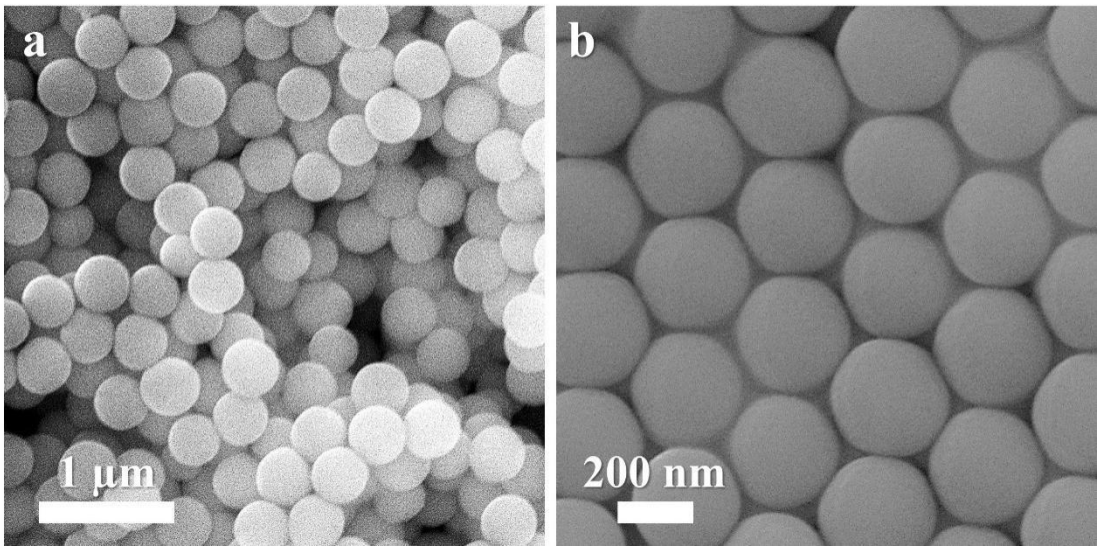

Fig. S1. SEM images of SiO_2 spheres.

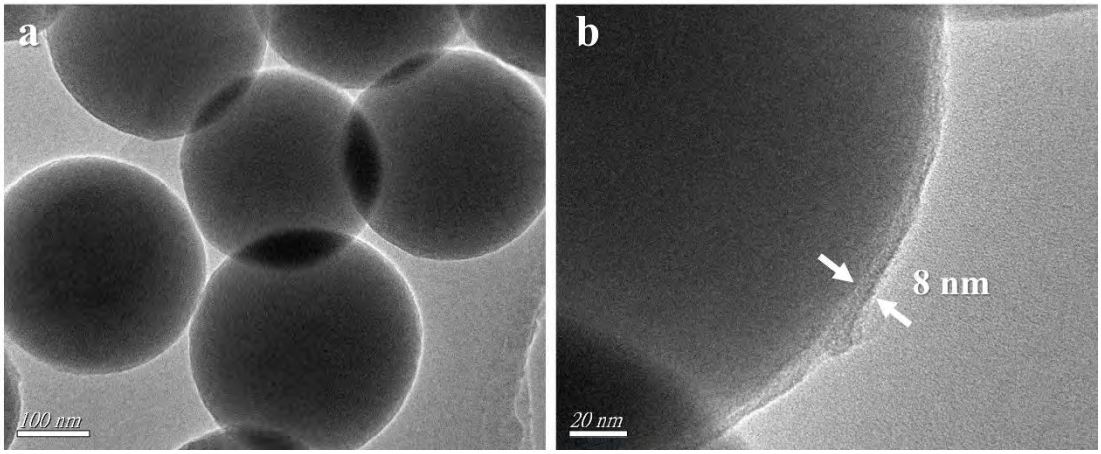

Fig. S2. TEM images of pyro-PDA@SiO_2.

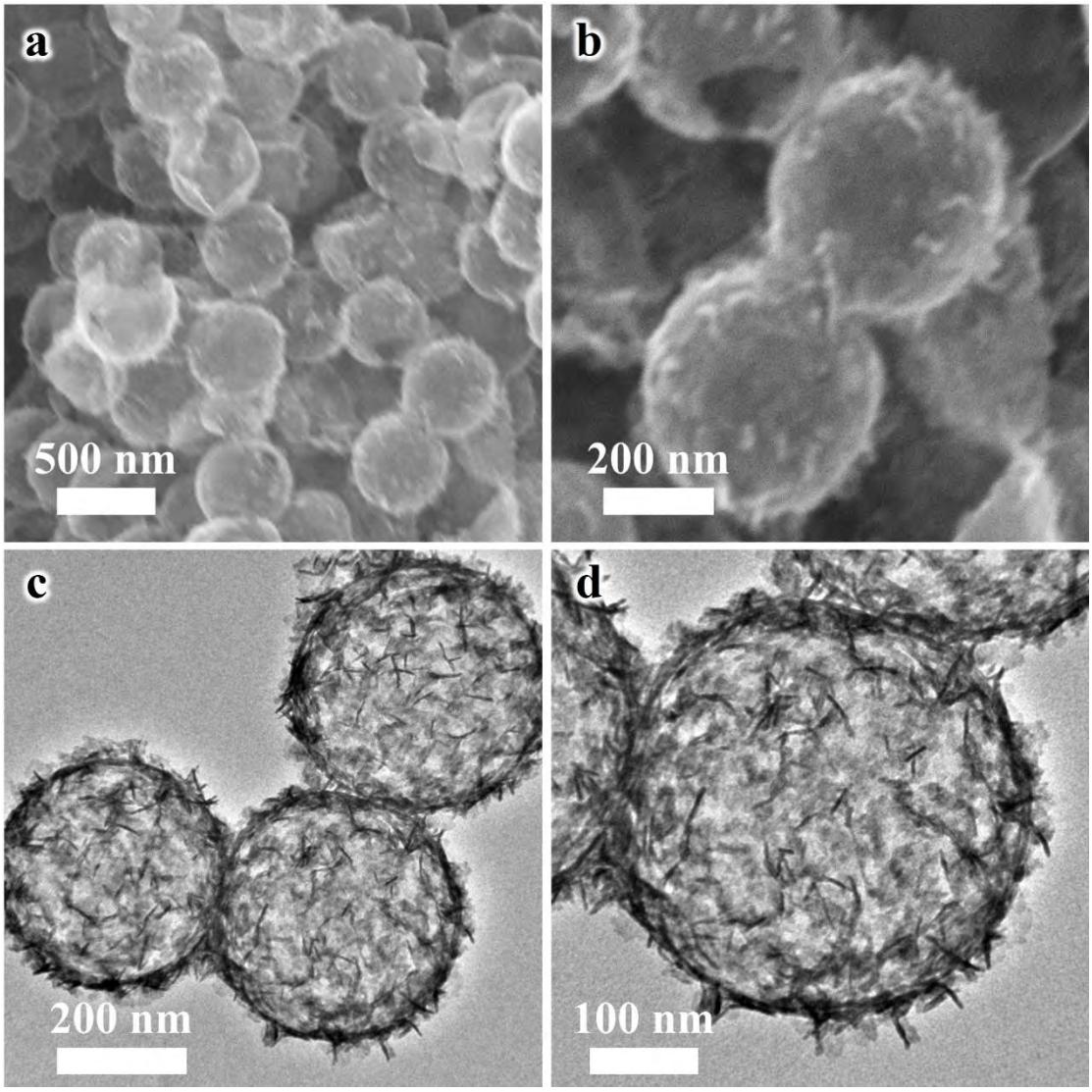

Fig. S3. (a-b) SEM images and (c-d) TEM images of BOB@NC-1.

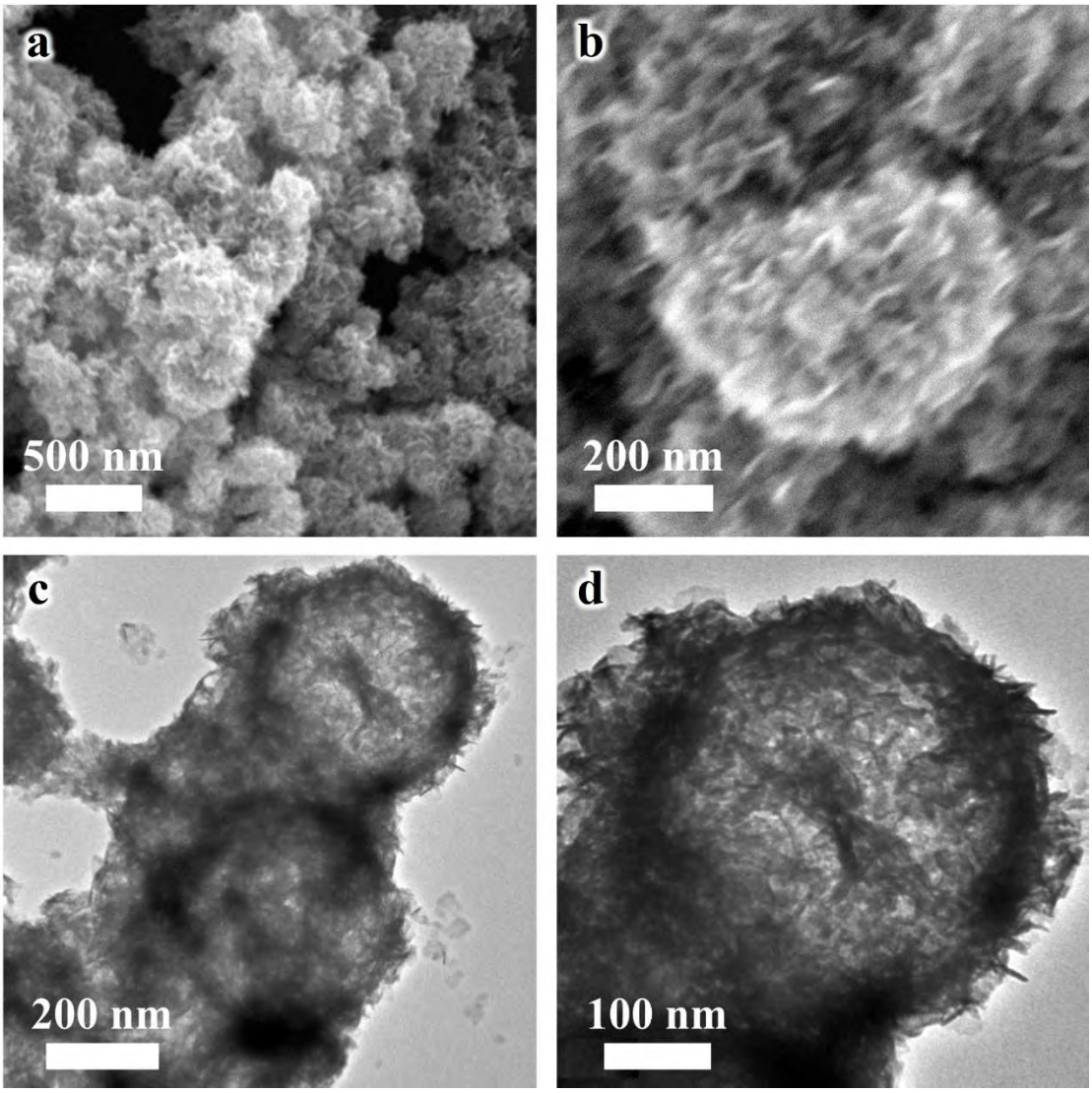

Fig. S4. (a-b) SEM images and (c-d) TEM images of BOB@NC-5.

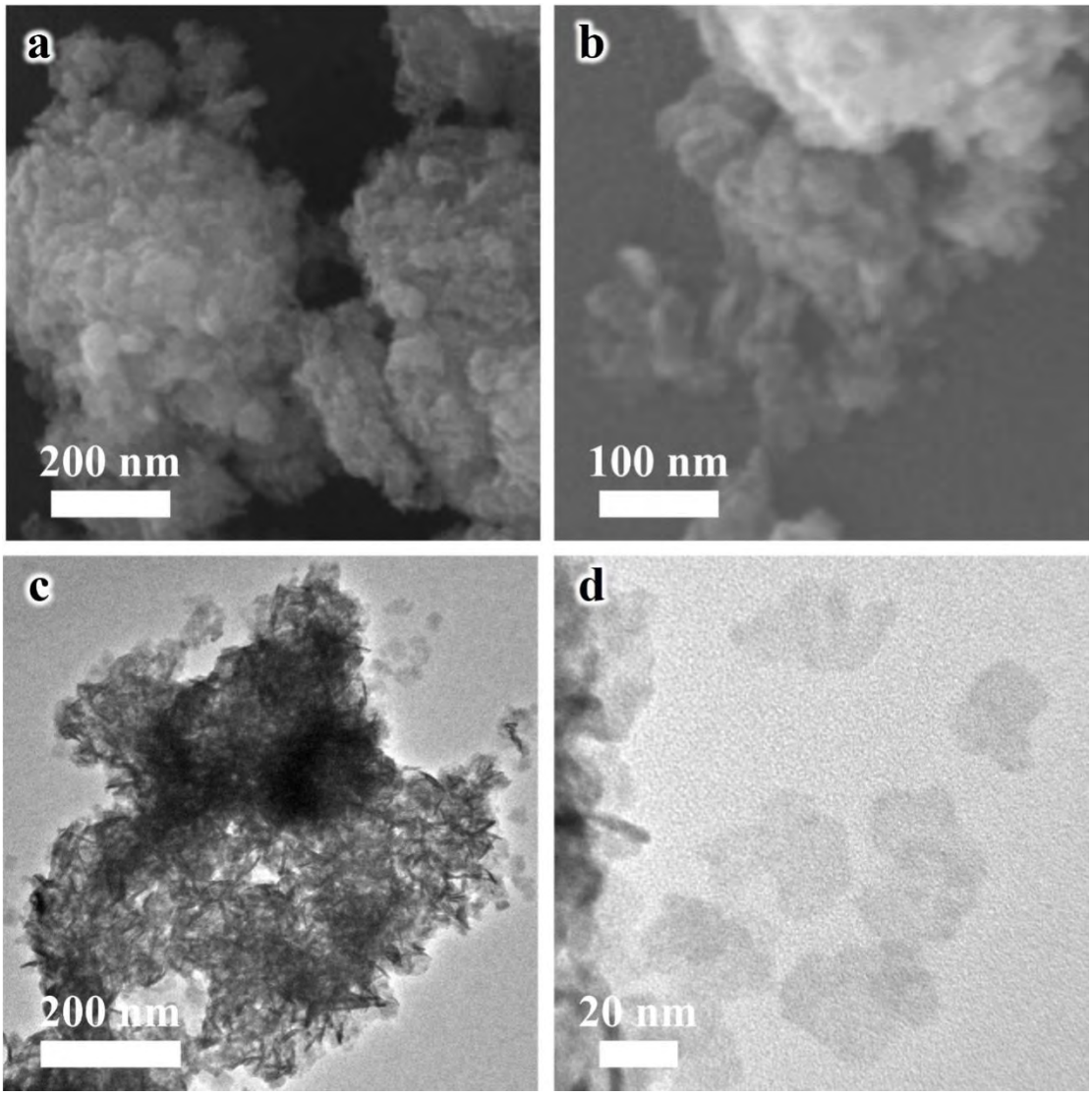

Fig. S5. (a-b) SEM images and (c-d) TEM images of BOB.

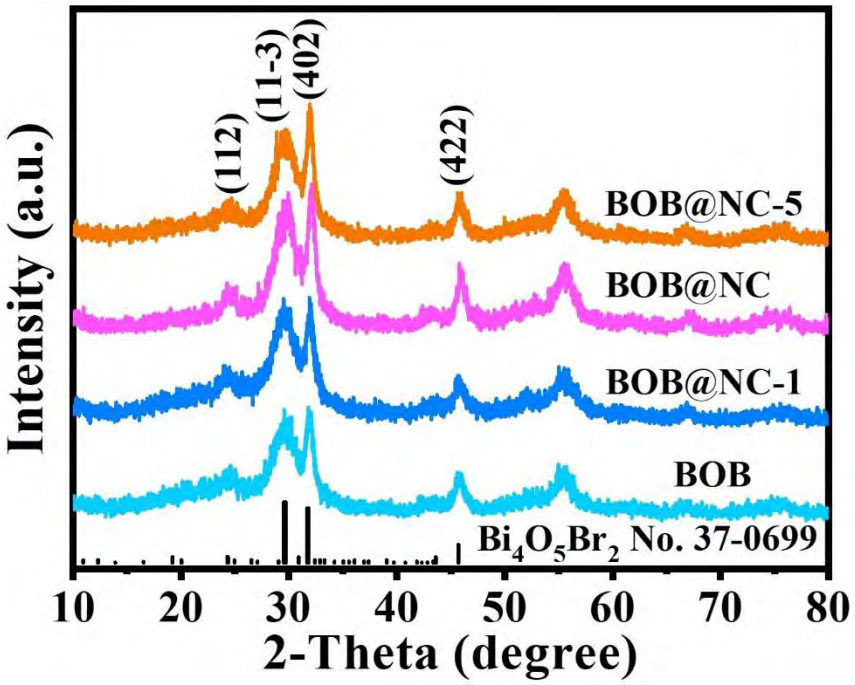

Fig. S6. XRD patterns of BOB and BOB@NC samples.

The phase structure of the samples is determined by XRD, which shows that BOB can be indexed to $Bi_4O_5Br_2$ (JCPDS card No. 37-0699). No characteristic peak of NC is observed from the XRD pattern of BOB@NC because of the weak signal from NC carbon and the small concentration of NC in the materials.

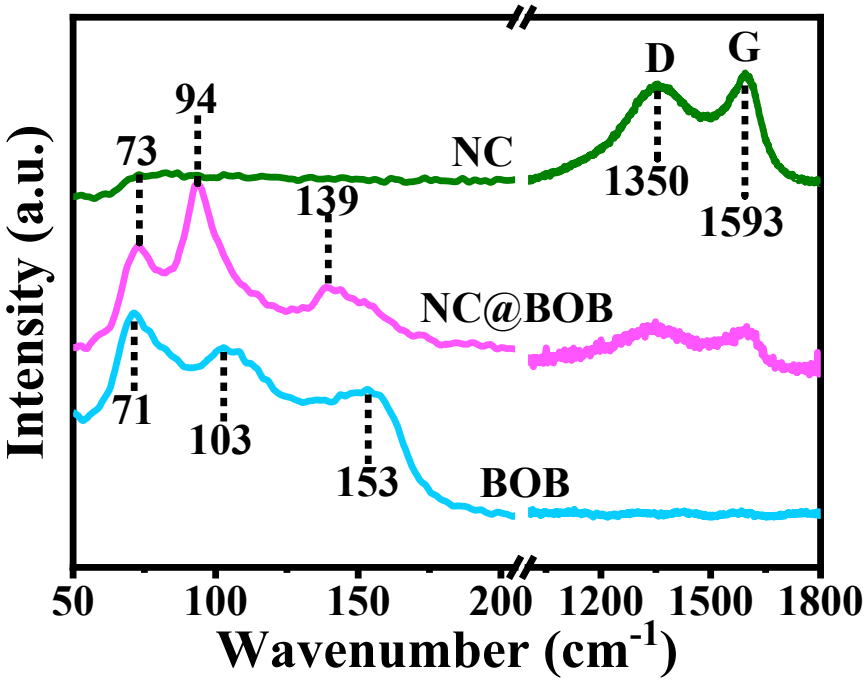

Fig. S7. Raman scattering spectra of NC, BOB, and BOB@NC.

Fig. S7 shows Raman bands at 71, 103, 153, 1,350, and 1,593 cm^{-1} representing the external A_{1g}, internal A_{1g}, E_{1g} internal Bi-Br stretching modes, defective carbon, as well as crystalline graphite bands, respectively. Compared to the monomeric NC and BOB, the Raman bands of the BOB@NC shift slightly attributable to the interactions between NC and BOB in BOB@NC.

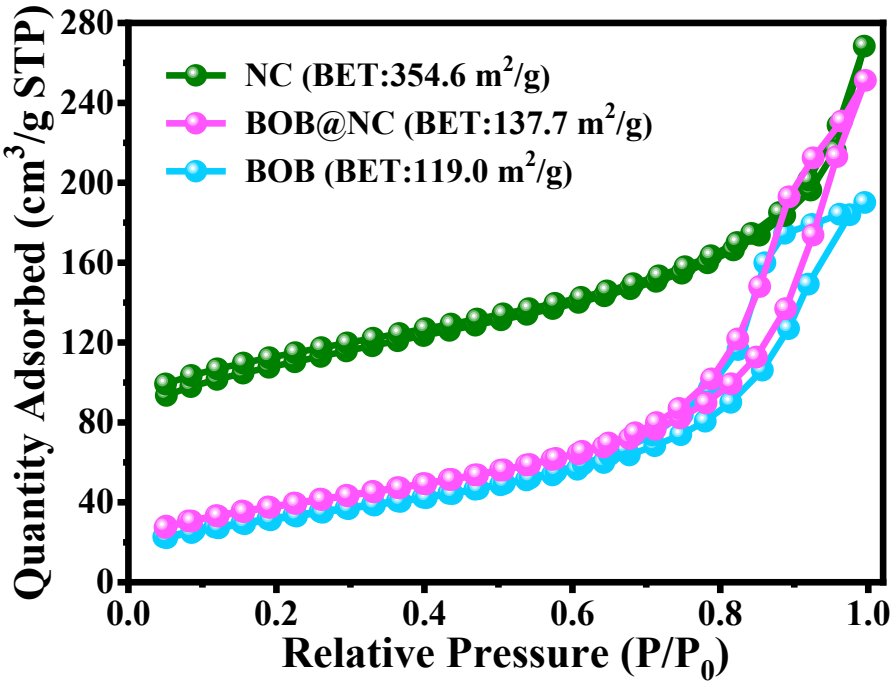

Fig. S8. N_2 adsorption-desorption isotherms of NC, BOB, and BOB@NC.

As shown in the N_2 adsorption-desorption isotherms of NC, BOB, and BOB@NC (**Fig. S8**), the BET specific surface areas of NC, BOB, and BOB@NC are 354.6, 137.7, and 119.0 m^2/g, respectively. The hollow-structured NC has the largest specific surface area, while the BOB monomer has a larger surface area than the traditional bismuth oxyhalide-based materials. Compared to the BOB monomer, the specific surface area of the BOB@NC-confined nanoreactor can be increased further by growing BOB nanosheets on the NC surface.

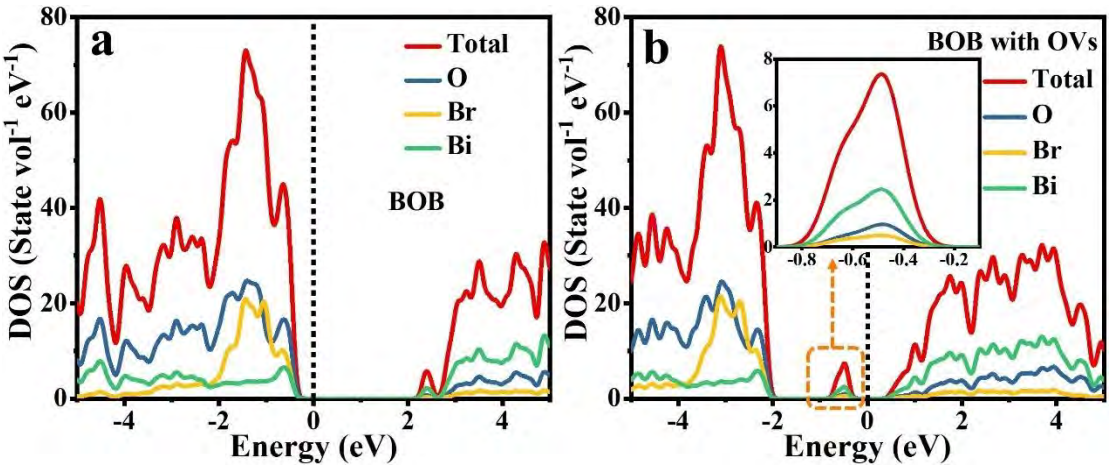

Fig. S9. Densities of states of BOB (a) without and (b) with oxygen vacancies (OVs).

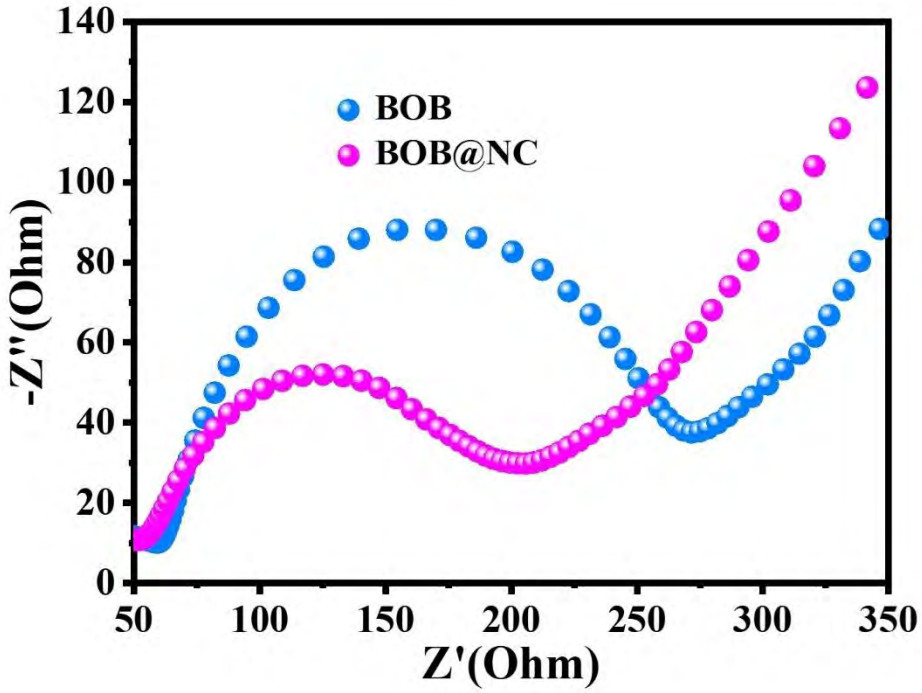

Fig. S10. Electrochemical impedance spectra of BOB and BOB@NC.

Fig. S10 shows the electrochemical impedance spectra (EIS) of BOB and BOB@NC. The diameter of the arc radius of BOB@NC is smaller than that of the pure BOB, suggesting that the interfacial layer resistance is on the surface of the electrode. The smaller arc radius signifies a higher efficiency for charge transfer. All in all, EIS indicates the BOB@NC nanoconfined reactor promotes the transfer and separation efficiency of photogenerated electron-hole pairs *via* the interactions between BOB and NC.

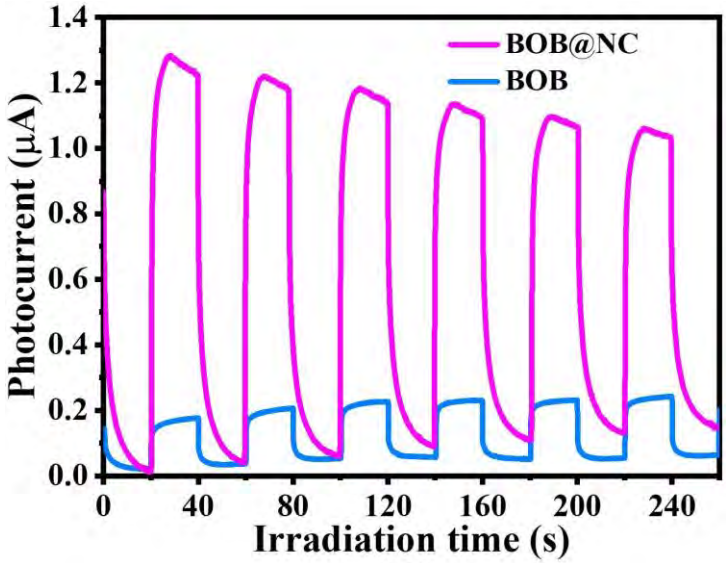

Fig. S11. Transient photocurrent spectra of BOB and BOB@NC.

Fig. S11 displays the transient photocurrent responses of pure BOB and BOB@NC upon light irradiation, revealing the generation of photocurrents with good reproducibility for six on-off cycles as well as good stability. The photocurrent of the BOB@NC nanoconfined reactor is about 6 times larger than that of the pure BOB under visible light irradiation, demonstrating reduced recombination of photoinduced electrons and holes on account of the interfacial interactions between BOB and NC.

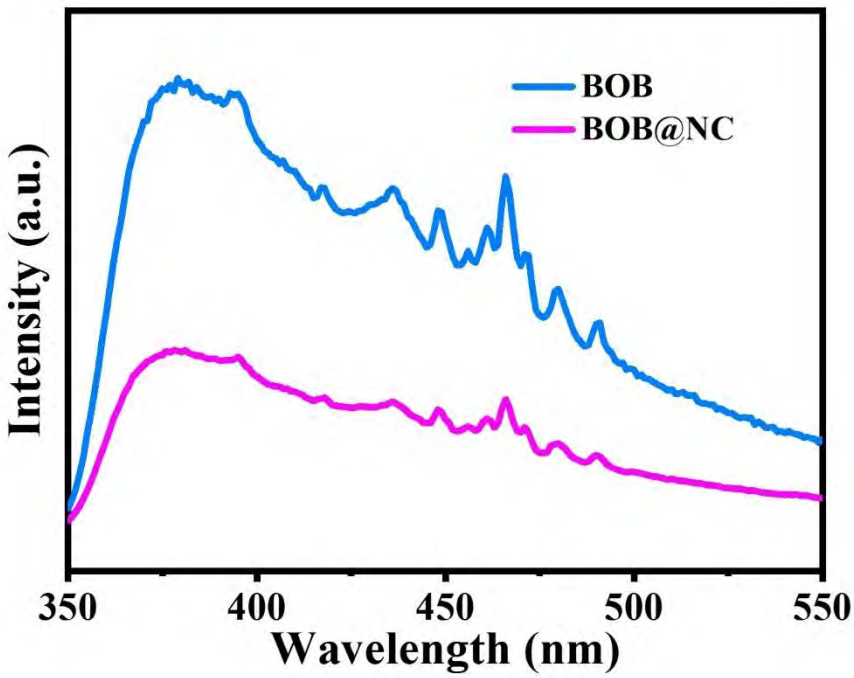

Fig. S12. Photoluminescence spectra of BOB and BOB@NC.

The transfer and recombination processes of photogenerated electrons are analyzed by photoluminescence (PL). **Fig. S12** exhibits the PL spectra of pure BOB and BOB@NC, and stronger emission is observed from BOB. The smaller PL intensity stems from a higher separation efficiency of photoexcited charge carriers, demonstrating that the BOB@NC nanoconfined reactor mitigates the recombination of electron-hole pairs efficiently and enhances the photocatalytic activity. The PL spectra are consistent with the electrochemical impedance spectra and transient photocurrent responses of these materials.

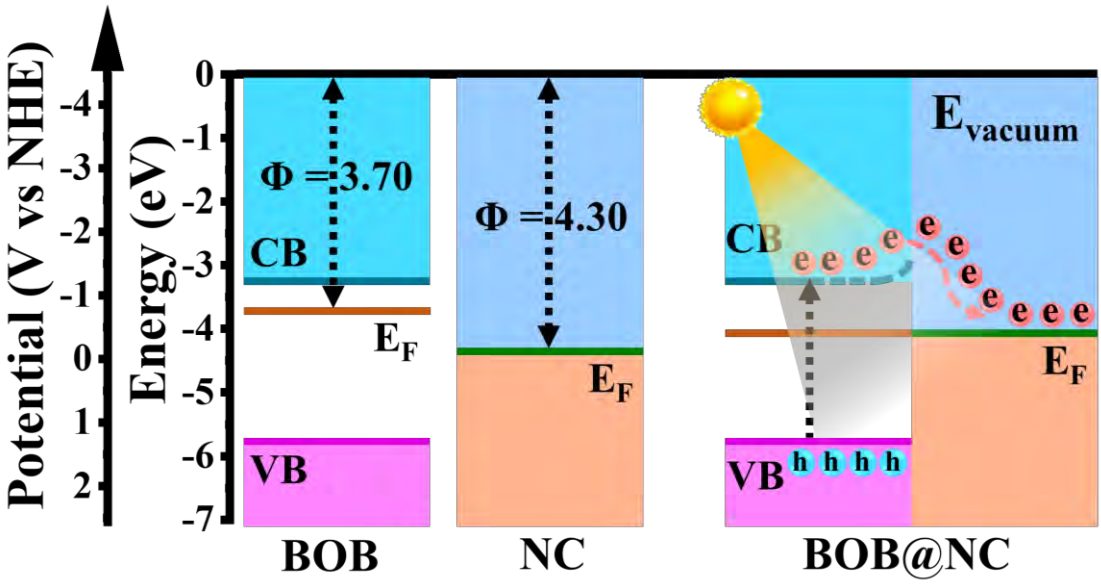

Fig. S13. Schematic diagram of the band structures of BOB, NC, and BOB@NC.

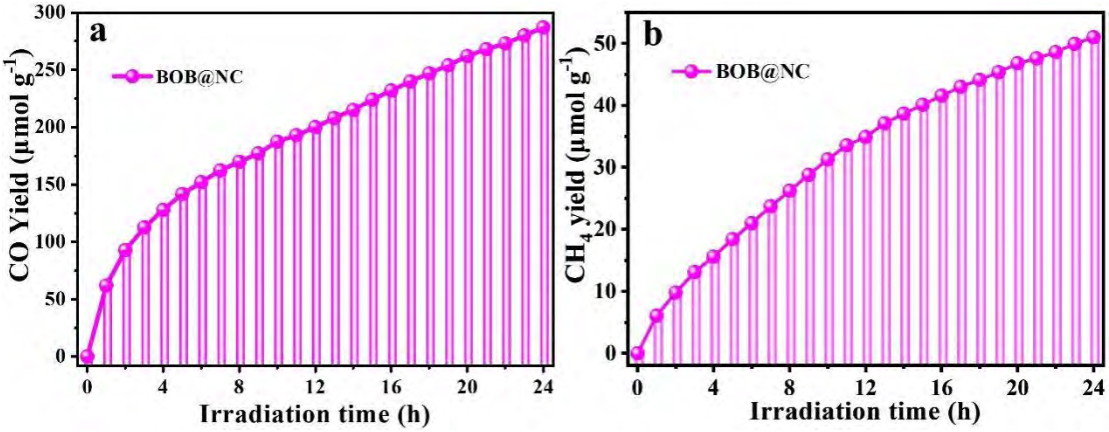

Fig. S14. (a) Photocatalytic CO evolution and (b) CH_4 evolution during light exposure for 24 hours.

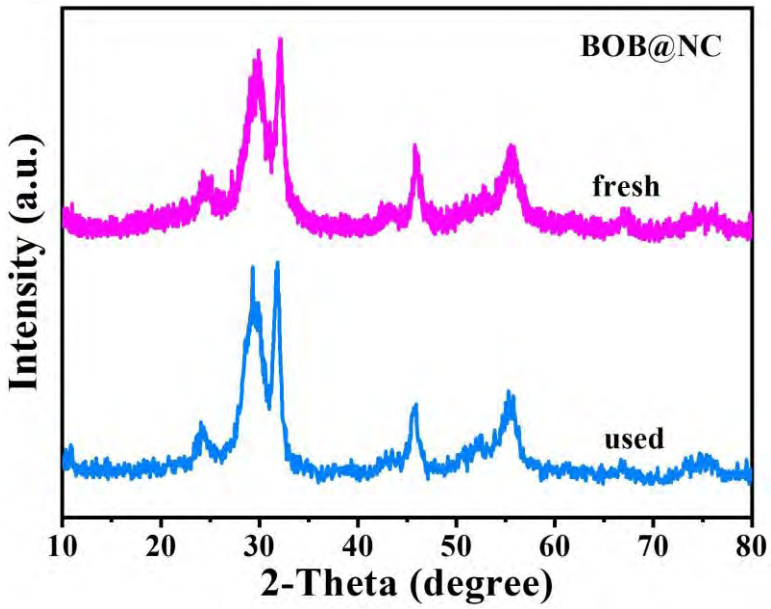

Fig. S15. XRD patterns of BOB@NC before and after photocatalytic CO_2 reduction.

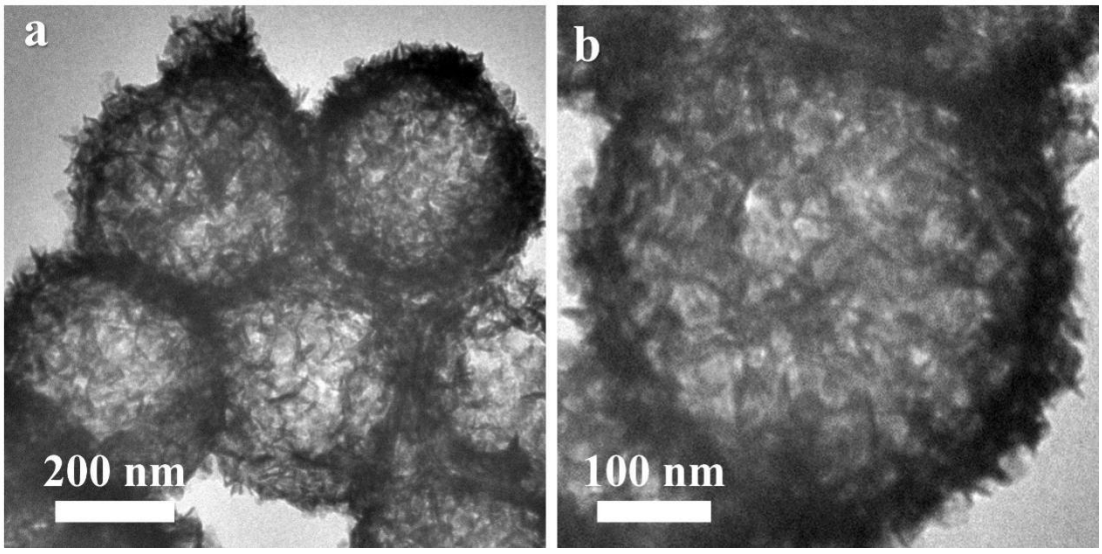

Fig. S16. TEM images of BOB@NC after photocatalytic CO_2 reduction.

Table S1. Comparison of the reaction conditions and characteristics of different photocatalysts pertaining to photocatalytic CO_2 conversion.

Photocatalysts	Dosages	Light sources	Products	Yields ($\mu mol\ g^{-1}\ h^{-1}$)	Refs.
BOB@NC	20 mg	300 W Xe lamp	CO/CH_4	28.34/3.68	**This work**
bismuthene	20 mg	300 W Xe lamp	CO/CH_4	14.32/4.69	*Adv. Mater.* **2024**, 36, 2312676
CuS atomic layers	5 mg	300 W Xe lamp $\lambda \geq 800$ nm	CO	14.5	*J. Am. Chem. Soc.* **2019**, 141, 423-430
HO-Ru/TiN	40 mg	300 W Xe lamp $\lambda \geq 800$ nm	CO	69	*J. Am. Chem. Soc.* **2023**, 145, 27415-27423
Vo-Rich WO_3 Atomic Layers	5 mg	300 W Xe lamp $\lambda \geq 800$ nm	CO	~2.75	*Joule* **2018**, 2, 1004-1016
CoS_2 nanosheets	5 mg	300 W Xe lamp $\lambda \geq 800$ nm	CH_4/CO	30.8/13.4	*Angew. Chem. Int. Ed.* **2021**, 60, 8705-8709
$Ag_2Cu_2O_3$ nanowires	30 mg	300 W Xe lamp	CH_4	3.55	*Angew. Chem. Int. Ed.* **2023**, 62, e2023096
$Cu_4(SO_4)(OH)_6$ nanosheets	5 mg	300 W Xe lamp $\lambda \geq 800$ nm	CO/CH_4	21.95/4.11	*Nat. Commun.* **2023**, 14, 4034.
Co_3O_4/CuO_x	-	300 W Xe lamp	CH_4	6.5 μmol h^{-1}	*ACS Nano* **2023**, 17, 11, 10976-10986
VS-$AgInS_2$ nanocrystals	20 mg	300 W Xe lamp $\lambda \geq 780$ nm	CO	8.04	*Appl. Catal. B Environ.* **2023**, 332, 122763.
Vo-rich MoO_{2-x}	20 mg	300 W Xe lamp	CH_4/CO	12.2/5.4	*Angew. Chem. Int. Ed.* **2023**, 62, e2022131
CoN porous atomic layers	20 mg	300 W Xe lamp $\lambda \geq 800$ nm	CO	0.29	*Nano Energy* **2020**, 69, 104421
$BiOBr_{0.6}Cl_{0.4}$ **BiOCl** **BiOBr**	10 mg	300 W Xe lamp	CO	15.86 2.11 1.55	*Appl. Catal. B Environ.* **2019**, 243, 734-740
CN-BiOBr-OV	10 mg	300 W Xe lamp	CO/CH_4	61.8/27.1	*Angew. Chem. Int. Ed.* **2020**, 59, 4519-4524
BiOBr **Co_2N/BiOBr-1**	30 mg	300 W Xe lamp	CO	11.2 67.8	*Nano Energy* **2021**, 79, 105429
BiOCl@Bi_2O_3 **BiOCl**	50 mg	300 W Xe lamp	CO	75 52	*Adv. Mater.* **2020**, 32, 2004311
C_3N_4/bismuthene/BiOCl	2 mg	300 W Xe lamp	CO/CH_4	71/61	*ACS Appl. Mater. Interfaces* **2021**, 13, 21582-21592
BiOCl-B-OV	50 mg	300 W Xe lamp $\lambda > 400$ nm	CO	83.64	*Adv. Mater.* **2021**, 33, 2100143

AgBr/BiOBr	10 mg	300 W Xe lamp	CO/CH_4	212.6/5.7	*Appl. Catal. B Environ.* **2022**, 301, 120802
VDWGs-rich BiOCl atomic layers	50 mg	300 W Xe lamp $\lambda > 400$ nm	CO	188.2	*Nat. Commun.* **2021**, 12, 5923
BiOBr-5	10 mg	300 W Xe lamp	CO	3.25	*Nano Energy* **2022**, 92, 106671
BiOCl-P	30 mg	300 W Xe lamp	CO/CH_4	19.52/0.76	*Small* **2022**, 18, 2105228
8 wt% CPDs/$Bi_4O_5Br_2$	30 mg	300 W Xe lamp	CO	132.42	*Appl. Catal. B Environ.* **2021**, 293, 120182
Bi_3O_4Cl/20%g-C_3N_4	50 mg	300 W Xe lamp	CO/CH_4	6.6/1.9	*Chem. Eng. J.* **2021**, 409, 128178
CPDs/$Bi_{12}O_{17}Cl_2$	30 mg	300 W Xe lamp $\lambda > 400$ nm	CO	3.2	*Chem. Eng. Sci.* **2021**, 232, 116338
$Bi_{12}O_{17}Cl_2$ nanotubes	30 mg	300 W Xe lamp	CO	48.6	*Angew. Chem. Int. Ed.* **2018**, 57, 14847-14851
V_{BiO}-$Bi_{24}O_{31}Br_{10}$	30 mg	300 W Xe lamp	CO	24.9	*Adv. Energy Mater.* **2021**, 11, 2102389
Co–Bi_3O_4Br-1	30 mg	300 W Xe lamp	CO	107.1	*Nat. Commun.* **2019**, 10, 2840
Sn-BiOBr/$BiOIO_3$	20 mg	300 W Xe lamp	CO	7.4	*Appl. Catal. B Environ.* **2021**, 298, 120618
$BiOIO_3$	20 mg	300 W Xe lamp	CO	2.09	*Appl. Catal. B Environ.* **2021**, 298, 120618
$BiOIO_3$-LOV2	20 mg	300 W Xe lamp	CO	17.33	*Adv. Mater.* **2020**, 32, 1908350
$BiOIO_3$-b3	50 mg	300 W Xe lamp	CO	5.42	*Adv. Funct. Mater.* **2018**, 28, 1804284
5 wt% CPDs/$PbBiO_2Br$	100 mg	300 W Xe lamp	CO	8.28	*Appl. Catal. B Environ.* **2019,** 254, 551-559
ROV $PbBiO_2Br$	20 mg	300 W Xe lamp	CO	4.58	*Appl. Catal. B Environ.* **2020**, 277, 119170